Available online at www.sciencedirect.com
ScienceDirect
Journal of Computational Physics 227 (2008) 2263–2285
JOURNAL OF COMPUTATIONAL PHYSICS
www.elsevier.com/locate/jcp

Conservative form of interpolated differential operator scheme for compressible and incompressible fluid dynamics

Yohsuke Imai [a,*], Takayuki Aoki [b], Kenji Takizawa [c]

[a] Department of Bioengineering and Robotics, Graduate School of Engineering, Tohoku University, 6-6-01 Aramaki Aza Aoba, Aoba-ku, Sendai-shi, Miyagi 980-8579, Japan
[b] Global Scientific Information and Computing Center, Tokyo Institute of Technology, 2-12-1O-Okayama, Meguro-ku, Tokyo 152-8550, Japan
[c] National Maritime Research Institute, 6-38-1 Shinkawa, Mitaka-shi, Tokyo 181-0004, Japan

Received 15 March 2007; received in revised form 27 September 2007; accepted 26 November 2007
Available online 9 January 2008

Abstract

The proposed scheme, which is a conservative form of the interpolated differential operator scheme (IDO-CF), can provide high accurate solutions for both compressible and incompressible fluid equations. Spatial discretizations with fourth-order accuracy are derived from interpolation functions locally constructed by both cell-integrated values and point values. These values are coupled and time-integrated by solving fluid equations in the flux forms for the cell-integrated values and in the derivative forms for the point values. The IDO-CF scheme exactly conserves mass, momentum, and energy, retaining the high resolution more than the non-conservative form of the IDO scheme. A direct numerical simulation of turbulence is carried out with comparable accuracy to that of spectral methods. Benchmark tests of Riemann problems and lid-driven cavity flows show that the IDO-CF scheme is immensely promising in compressible and incompressible fluid dynamics studies.

PACS: 02.60.−x; 02.60.Cb; 02.70.−c

Keywords: IDO scheme; Conservative form; Computational fluid dynamics; High resolution

1. Introduction

In many problems of complex flows involving turbulence, multi-phase fluid, and fluid–structure interaction, numerical schemes are required to resolve a wide range of wavenumbers, and the use of multi-moment schemes would be one of the successful solutions. Multi-moments, that is, not only point value of a physical variable but also its spatial derivative or cell-integrated value, are time-integrated as dependent variables of governing equations. In constrained interpolation profile (CIP) scheme [1,2], which is a multi-moment

* Corresponding author. Tel.: +81 22 714 8514; fax: +81 22 795 6958.
E-mail address: yimai@pfsl.mech.tohoku.ac.jp (Y. Imai).

0021-9991/$ - see front matter © 2007 Elsevier Inc. All rights reserved.
doi:10.1016/j.jcp.2007.11.031

semi-Lagrangian scheme of hyperbolic equations, solution profile in a cell is approximated by local third-order Hermite interpolation function, constructed by the point values and the spatial derivatives. Even for high wavenumbers, since the interpolation function becomes good approximated profile, both the wave speed and amplitude are accurately estimated by the semi-Lagrangian procedure [3]. The CIP scheme has extensively contributed to analyses of scientific and engineering problems [4–8].

Interpolated differential operator (IDO) scheme [9,10], which is also based on multi-moments time integration, is an Eulerian scheme for solving hyperbolic, parabolic, and elliptic equations. Fluid equations described by the primitive variables are discretized in non-conservative forms by applying differential operators to local interpolation functions. The IDO scheme has higher resolution property than fourth-order compact difference (CD) scheme [11] for all the terms of fluid equations [12], and that makes it possible to obtain comparable results with spectral methods for direct numerical simulation (DNS) of uniform isotropic turbulence [13]. A disadvantage of the IDO scheme is a lack of exact conservation. Although conservation of numerical solutions is kept well and practically acceptable [14], exact conservation is required in some cases such as shock capturing, multi-phase flow and long-time integration.

Finite volume (FV) formulation, which represents fluid equations for cell-integrated values in flux form, is inherently conservative. In recent years, high-order FV schemes based on compact difference approach have been reported [15–17]. In also CIP framework, conservative schemes have been proposed [18–20], in which cell-integrated value and point value are used as multi-moments. The conservative schemes, so-called CIP conservative semi-Lagrangian (CIP–CSL) employ flux form discretization for the cell-integrated value while the point value is calculated in non-conservative form. The CIP–CSL schemes and its extension to FV formulation [21] have demonstrated some superior results to the conventional CIP scheme, particularly in analyzing multi-phase flows [22]. In multi-dimensional cases, semi-Lagrangian procedure of the CIP–CSL schemes has difficulty estimating advection fluxes from multi-dimensional interpolation, and thus alternatively directional splitting is adopted. The directional splitting however introduces phase errors to the numerical results.

We propose the IDO scheme in conservative form (IDO-CF) using the cell-integrated values and the point values in multi-moments time integration as well as the CIP–CSL schemes. In contrast to the CIP–CSL schemes, Eulerian approach of the IDO-CF scheme straightforwardly discretizes multi-dimensional fluid equations without directional splitting. Moreover, high-order discretizations of both advection and non-advection terms with the same procedure can promise highly resolved solutions for complex flow problems. Although the proposed scheme may be applicable to any partial differential equations, the paper focuses on compressible and incompressible fluid equations.

2. The IDO-CF scheme

We consider the conservation laws for compressible fluid in one-dimension:

$$\frac{\partial \mathbf{Q}}{\partial t}+\frac{\partial \mathbf{F}}{\partial x}=0,\qquad \mathbf{Q}=\begin{bmatrix}\rho\\ m\\ e\end{bmatrix},\quad \mathbf{F}=\begin{bmatrix}\rho u\\ mu+p\\ eu+pu\end{bmatrix}, \tag{1}$$

where the notation t refers to the time, x the spatial coordinate, ρ the density, $m=\rho u$ the momentum, e the total energy, u the velocity and p is the pressure. The one-dimensional computational domain is divided into finite-number cells in which the cell i is defined with the cell interfaces $i-1/2$ and $i+1/2$, where $i=1,2,\ldots,N$. In the IDO-CF scheme, the cell-integrated value (line-integrated value in one-dimensional case) ${}^{x}\mathbf{Q}_i \equiv \int_{x_{i-1/2}}^{x_{i+1/2}} \mathbf{Q}\,\mathrm{d}x$ is time-integrated at the cell i as a dependent variable. We adopt collocated grid configuration, that is, the cell-integrated values of the density, the momentum, and the energy are defined at the same location for the cell. Integrating Eq. (1) over the cell i, we have semi-discretized equation for the cell-integrated value:

$$\frac{\partial}{\partial t}{}^{x}\mathbf{Q}_i=-\mathbf{F}_{i+1/2}+\mathbf{F}_{i-1/2}. \tag{2}$$

The IDO-CF scheme also defines the point value $\mathbf{Q}_{i+1/2}$ at the cell interface (grid point) $i+1/2$ as an additional time-integrated variable. For the point value, Eq. (1) leads to

$$\frac{\partial}{\partial t}\mathbf{Q}_{i+1/2} = -\frac{\partial \mathbf{F}}{\partial x_{i+1/2}}. \tag{3}$$

Both the equations are solved as coupled equations. While Eq. (3) for the point value is solved in the non-conservative form, Eq. (2) for the cell-integrated value is in the flux form. Thus, the cell-integrated values of mass, momentum, and total energy are exactly conserved. The cell-integrated values and point values of primitive variables u and p can be calculated by using the time-integrated variables ρ, m and e. The fluxes in Eq. (2) are simply discretized by substituting the point values given at the cell interface:

$$\mathbf{F}_{i+1/2} = \begin{bmatrix} \rho_{i+1/2}u_{i+1/2} \\ m_{i+1/2}u_{i+1/2} + p_{i+1/2} \\ e_{i+1/2}u_{i+1/2} + p_{i+1/2}u_{i+1/2} \end{bmatrix}. \tag{4}$$

The right-hand side of Eq. (3), however, contains unknown spatial derivatives as follows:

$$\frac{\partial \mathbf{F}}{\partial x_{i+1/2}} = \begin{bmatrix} u_{i+1/2}\frac{\partial \rho}{\partial x_{i+1/2}} + \rho_{i+1/2}\frac{\partial u}{\partial x_{i+1/2}} \\ u_{i+1/2}\frac{\partial m}{\partial x_{i+1/2}} + m_{i+1/2}\frac{\partial u}{\partial x_{i+1/2}} + \frac{\partial p}{\partial x_{i+1/2}} \\ u_{i+1/2}\frac{\partial e}{\partial x_{i+1/2}} + e_{i+1/2}\frac{\partial u}{\partial x_{i+1/2}} + u_{i+1/2}\frac{\partial p}{\partial x_{i+1/2}} + p_{i+1/2}\frac{\partial u}{\partial x_{i+1/2}} \end{bmatrix}. \tag{5}$$

These derivatives must be approximated. We apply two kinds of discretization method selectively, taking account of the flow characteristics: central discretization and upwind discretization. Eq. (5) is then rewritten as

$$\frac{\partial \mathbf{F}}{\partial x_{i+1/2}} = \begin{bmatrix} u_{i+1/2}\frac{\partial \rho^{\mathrm{UP}}}{\partial x_{i+1/2}} + \rho_{i+1/2}\frac{\partial u^{\mathrm{C}}}{\partial x_{i+1/2}} \\ u_{i+1/2}\frac{\partial m^{\mathrm{UP}}}{\partial x_{i+1/2}} + m_{i+1/2}\frac{\partial u^{\mathrm{C}}}{\partial x_{i+1/2}} + \frac{\partial p^{\mathrm{C}}}{\partial x_{i+1/2}} \\ u_{i+1/2}\frac{\partial e^{\mathrm{UP}}}{\partial x_{i+1/2}} + e_{i+1/2}\frac{\partial u^{\mathrm{C}}}{\partial x_{i+1/2}} + u_{i+1/2}\frac{\partial p^{\mathrm{C}}}{\partial x_{i+1/2}} + p_{i+1/2}\frac{\partial u^{\mathrm{C}}}{\partial x_{i+1/2}} \end{bmatrix}, \tag{6}$$

where the superscript C and UP represent the central discretization and the upwind discretization described in the following section.

2.1. Derivative discretization

According to the concept of the IDO scheme [9], discretized expressions for spatial derivatives of a variable $\phi(x)$ are derived from an interpolation function $\Phi(X)$ constructed in local domain by using both the cell-integrated values and the point values, where $X = x - x_{i+1/2}$. When the interpolation function is accurate enough, the spatial profile of $\phi(x)$ in local domain can be approximated as $\phi(x) \approx \Phi(X)$. Differentiating the interpolation function, we have also spatial profile of derivatives. By substituting $X = 0$, the derivatives at the cell-interface is expressed as

$$\frac{\partial^k \phi}{\partial x^k}_{i+1/2} = \frac{\partial^k \Phi}{\partial X^k}_{i+1/2}, \tag{7}$$

where the notation k represents an order of derivative. Although many mathematical functions are applicable to the interpolation function, in this paper we use a high-order polynomial:

$$\Phi(X) = \sum_k A_k X^k \tag{8}$$

and the derivative approximation (7) reduces to

$$\frac{\partial^k \phi}{\partial x^k}_{i+1/2} = \frac{\partial^k \Phi}{\partial X^k}_{i+1/2} = k! A_k. \tag{9}$$

2.1.1. Central discretization

For the central discretizations, the interpolation function covers the both-side cells from the viewpoint of $x = x_{i+1/2}$. The IDO-CF scheme uses the following fourth-order polynomial for the local domain $x_{i-1/2} \leqslant x \leqslant x_{i+3/2}$:

$$\Phi^{\mathrm{C}}(X) = a_4X^4 + a_3X^3 + a_2X^2 + a_1X + \phi_{i+1/2}, \tag{10}$$

where the superscript C represents the interpolation function for the central discretizations. The four unknown coefficients of Eq. (10) can be determined by the four constraints $\Phi^{\mathrm{C}}(h_p) = \phi_{i+3/2}$, $\Phi^{\mathrm{C}}(-h_m) = \phi_{i-1/2}$, $\int_{-h_m}^{0} \Phi^{\mathrm{C}}\,\mathrm{d}X = {}^x\phi_i$, and $\int_0^{h_p} \Phi^{\mathrm{C}}\,\mathrm{d}X = {}^x\phi_{i+1}$, where $h_p = x_{i+3/2} - x_{i+1/2}$ and $h_m = x_{i+1/2} - x_{i-1/2}$. In the case of the uniform meshes $h_p = h_m = h$, we have the central discretizations of derivatives using Eq. (9):

$$\left(\frac{\partial\phi}{\partial x}\right)^{\mathrm{C}}_{i+1/2} = \frac{2}{h^2}({}^x\phi_{i+1} - {}^x\phi_i) - \frac{1}{2h}(\phi_{i+3/2} - \phi_{i-1/2}), \tag{11}$$

$$\left(\frac{\partial^2\phi}{\partial x^2}\right)^{\mathrm{C}}_{i+1/2} = \frac{15}{2h^3}({}^x\phi_{i+1} + {}^x\phi_i) - \frac{3}{2h^2}(\phi_{i+3/2} + 8\phi_{i+1/2} + \phi_{i-1/2}), \tag{12}$$

$$\left(\frac{\partial^3\phi}{\partial x^3}\right)^{\mathrm{C}}_{i+1/2} = -\frac{12}{h^4}({}^x\phi_{i+1} - {}^x\phi_i) + \frac{6}{h^3}(\phi_{i+3/2} - \phi_{i-1/2}), \tag{13}$$

$$\left(\frac{\partial^4\phi}{\partial x^4}\right)^{\mathrm{C}}_{i+1/2} = -\frac{90}{h^5}({}^x\phi_{i+1} + {}^x\phi_i) + \frac{30}{h^4}(\phi_{i+3/2} + 4\phi_{i+1/2} + \phi_{i-1/2}). \tag{14}$$

The truncation errors of these discretizations are described in Appendix 1.

2.1.2. Upwind discretization

The central discretization can cause numerical oscillations in the calculation of advection terms, in particular for high wavenumber profile. The upwind discretization is used for avoiding the numerical oscillations. Considering characteristics of the advection, we construct the upwind interpolation function $\Phi^{\mathrm{UP}}(X)$ for a half-side cell in the upwind direction, which is used in CIP–CSL2 scheme [19]:

$$\Phi^{\mathrm{UP}}(X) = b_2X^2 + b_1X + \phi_{i+1/2}. \tag{15}$$

If the advection velocity u is negative at the cell surface $i + 1/2$, the constraints of $\Phi^{\mathrm{UP}}(h)=\phi_{i+3/2}$ and $\int_0^h \Phi^{\mathrm{UP}}\,\mathrm{d}X = {}^x\phi_{i+1}$ determine the coefficients b_1 and b_2 in Eq. (15) and the following discretizations are derived:

$$\left(\frac{\partial\phi}{\partial x}\right)^{\mathrm{UP}}_{i+1/2} = \frac{6}{h^2}{}^x\phi_{i+1} - \frac{2}{h}(\phi_{i+3/2} + 2\phi_{i+1/2}), \tag{16}$$

$$\left(\frac{\partial^2\phi}{\partial x^2}\right)^{\mathrm{UP}}_{i+1/2} = -\frac{12}{h^3}{}^x\phi_{i+1} + \frac{6}{h^2}(\phi_{i+3/2} + \phi_{i+1/2}). \tag{17}$$

On the other hand, the advection velocity is positive, we have

$$\left(\frac{\partial\phi}{\partial x}\right)^{\mathrm{UP}}_{i+1/2} = -\frac{6}{h^2}{}^x\phi_i + \frac{2}{h}(2\phi_{i+1/2} + \phi_{i-1/2}), \tag{18}$$

$$\left(\frac{\partial^2\phi}{\partial x^2}\right)^{\mathrm{UP}}_{i+1/2} = -\frac{12}{h^3}{}^x\phi_i + \frac{6}{h^2}(\phi_{i+1/2} + \phi_{i-1/2}) \tag{19}$$

with the constraints of $\Phi^{\mathrm{UP}}(-h)=\phi_{i-1/2}$ and $\int_{-h}^{0} \Phi^{\mathrm{UP}}\,\mathrm{d}X = {}^x\phi_i$. The upwind discretization includes numerical viscosity shown in Appendix 2.

2.2. Primitive variable

The non-conservative primitive variables u and p appear in the flux terms of the Euler equations (1). In general, the pressure is determined by the equation of state (EOS) as functions of the density and the internal energy per unit mass $\varepsilon = e/\rho - u^2/2$:

$$p = \mathrm{EOS}(\rho, \varepsilon). \tag{20}$$

When the fluid is assumed to be ideal gas, the EOS is

$$p = (\gamma - 1)\rho\varepsilon, \tag{21}$$

where the notation γ is the specific heat ratio. The point values of the primitive variables are simply calculated by using the given point values of the density, the momentum, and the total energy:

$$u_{i+1/2} = \frac{m_{i+1/2}}{\rho_{i+1/2}}, \quad p_{i+1/2} = \mathrm{EOS}\left(\rho_{i+1/2}, \frac{e_{i+1/2}}{\rho_{i+1/2}} - \frac{u_{i+1/2}^2}{2}\right). \tag{22}$$

In the calculation of the cell-integrated values of the primitive variables

$${}^x u_i = {}^x\left(\frac{m}{\rho}\right)_i, \quad {}^x p_i = {}^x\mathrm{EOS}(\rho, \varepsilon)_i, \tag{23}$$

we apply the Simpson integration. First, the point values of the density, the momentum, and the energy at the cell-centered point are interpolated using CIP–CSL2 interpolation function covering the cell:

$$\Phi^{\mathrm{IN}}(X) = c_2 X^2 + c_1 X + c_0, \tag{24}$$

where $X = x - x_{i-1/2}$. From the constraints of $\Phi^{\mathrm{IN}}(0) = \phi_{i-1/2}$, $\Phi^{\mathrm{IN}}(h) = \phi_{i+1/2}$, and $\int_0^h \Phi^{\mathrm{IN}}\,\mathrm{d}X = {}^x\phi_i$, we have

$$\Phi^{\mathrm{IN}}(X) = \left(-6\left(\frac{X}{h}\right)^2 + 6\left(\frac{X}{h}\right)\right)\frac{{}^x\phi_i}{h} + \left(3\left(\frac{X}{h}\right)^2 - 2\left(\frac{X}{h}\right)\right)\phi_{i+1/2} + \left(3\left(\frac{X}{h}\right)^2 - 4\left(\frac{X}{h}\right) + 1\right)\phi_{i-1/2}. \tag{25}$$

By substituting $X = h/2$ into Eq. (25), the cell-centered value ϕ_{ic}^{IN} is interpolated as

$$\phi_{ic}^{\mathrm{IN}} = \frac{3}{2}\frac{{}^x\phi_i}{h} - \frac{1}{4}(\phi_{i+1/2} + \phi_{i-1/2}), \tag{26}$$

where the truncation error is fourth-order as shown in Appendix 3. The cell-centered values of ρ_{ic}^{IN}, m_{ic}^{IN}, and e_{ic}^{IN} give the cell-centered values of the velocity and the pressure:

$$u_{ic}^{\mathrm{IN}} = \frac{m_{ic}^{\mathrm{IN}}}{\rho_{ic}^{\mathrm{IN}}}, \quad p_{ic}^{\mathrm{IN}} = \mathrm{EOS}(\rho_{ic}^{\mathrm{IN}}, \varepsilon_{ic}^{\mathrm{IN}}), \tag{27}$$

where

$$\varepsilon_{ic}^{\mathrm{IN}} = \frac{e_{ic}^{\mathrm{IN}}}{\rho_{ic}^{\mathrm{IN}}} - \frac{(u_{ic}^{\mathrm{IN}})^2}{2}. \tag{28}$$

Then, the Simpson integration leads to

$${}^x u_i = \frac{h}{6}(u_{i+1/2} + 4u_{ic}^{\mathrm{IN}} + u_{i-1/2}), \quad {}^x p_i = \frac{h}{6}(p_{i+1/2} + 4p_{ic}^{\mathrm{IN}} + p_{i-1/2}). \tag{29}$$

This procedure can be applied even to a tabular EOS. The truncation errors of the primitive variables are presented in Appendix 4.

2.3. Time integration

A simple way to time-integrate Eqs. (2) and (3) with high accuracy is to use the Runge–Kutta method:

$${}^x\mathbf{Q}_i^{n+1} = {}^x\mathbf{Q}_i^n + \sum_p \beta_p\, {}^x\mathbf{k}_i^p \Delta t, \tag{30}$$

$$\mathbf{Q}_{i+1/2}^{n+1} = \mathbf{Q}_{i+1/2}^n + \sum_p \beta_p \mathbf{k}_{i+1/2}^p \Delta t, \tag{31}$$

where

$${}^x\mathbf{k}_i^p = \frac{\partial}{\partial t}\,{}^x\mathbf{Q}_i^p, \tag{32}$$

$$\mathbf{k}_{i+1/2}^p = \frac{\partial}{\partial t}\mathbf{Q}_{i+1/2}^p, \tag{33}$$

$$ {}^{x}\mathbf{Q}_i^p = {}^{x}\mathbf{Q}_i^n + \sum_q \alpha_{pq}\, {}^{x}\mathbf{k}_i^q \Delta t, \tag{34} $$

$$ \mathbf{Q}_{i+1/2}^p = \mathbf{Q}_{i+1/2}^n + \sum_q \alpha_{pq} \mathbf{k}_{i+1/2}^q \Delta t, \tag{35} $$

${}^{x}\mathbf{k}_i^p$ and $\mathbf{k}_{i+1/2}^p$ are the time derivatives in the stage number p of the Runge–Kutta method, α_{pq} and β_p are weighted coefficients, and n is the time step index. We use the following coefficients:

For the first-order method, being identical to the first-order finite difference in time:

$$ p = 1, \quad \alpha_{11} = 0, \quad \beta_1 = 1. \tag{36} $$

For the second-order method:

$$ p = 1, 2, \quad \begin{pmatrix} \alpha_{11} & \alpha_{12} \\ \alpha_{21} & \alpha_{22} \end{pmatrix} = \begin{pmatrix} 0 & 0 \\ 1 & 0 \end{pmatrix}, \quad \begin{pmatrix} \beta_1 \\ \beta_2 \end{pmatrix} = \begin{pmatrix} 1/2 \\ 1/2 \end{pmatrix}. \tag{37} $$

For the third-order method:

$$ p = 1, 2, 3, $$

$$ \begin{pmatrix} \alpha_{11} & \alpha_{12} & \alpha_{13} \\ \alpha_{21} & \alpha_{22} & \alpha_{23} \\ \alpha_{31} & \alpha_{32} & \alpha_{33} \end{pmatrix} = \begin{pmatrix} 0 & 0 & 0 \\ 2/3 & 0 & 0 \\ 0 & 2/3 & 0 \end{pmatrix}, \quad \begin{pmatrix} \beta_1 \\ \beta_2 \\ \beta_3 \end{pmatrix} = \begin{pmatrix} 1/4 \\ 3/8 \\ 3/8 \end{pmatrix}. \tag{38} $$

For the fourth-order method:

$$ p = 1, 2, 3, 4, $$

$$ \begin{pmatrix} \alpha_{11} & \alpha_{12} & \alpha_{13} & \alpha_{14} \\ \alpha_{21} & \alpha_{22} & \alpha_{23} & \alpha_{24} \\ \alpha_{31} & \alpha_{32} & \alpha_{33} & \alpha_{34} \\ \alpha_{41} & \alpha_{42} & \alpha_{43} & \alpha_{44} \end{pmatrix} = \begin{pmatrix} 0 & 0 & 0 & 0 \\ 1/2 & 0 & 0 & 0 \\ 0 & 1/2 & 0 & 0 \\ 0 & 0 & 1 & 0 \end{pmatrix}, \quad \begin{pmatrix} \beta_1 \\ \beta_2 \\ \beta_3 \\ \beta_4 \end{pmatrix} = \begin{pmatrix} 1/6 \\ 1/3 \\ 1/3 \\ 1/6 \end{pmatrix}. \tag{39} $$

2.4. Multi-dimension

The IDO-CF scheme in one-dimension can be extended to multi-dimensional problems straightforwardly. Consider the two-dimensional Euler equations for compressible fluid:

$$ \frac{\partial \mathbf{Q}}{\partial t} + \frac{\partial \mathbf{E}}{\partial x} + \frac{\partial \mathbf{F}}{\partial y} = 0, $$

$$ \mathbf{Q} = \begin{bmatrix} \rho \\ m_x \\ m_y \\ e \end{bmatrix}, \quad \mathbf{E} = \begin{bmatrix} \rho u \\ m_x u + p \\ m_y u \\ eu + pu \end{bmatrix}, \quad \mathbf{F} = \begin{bmatrix} \rho v \\ m_x v \\ m_y v + p \\ ev + pv \end{bmatrix}, \tag{40} $$

where $m_x = \rho u$ and $m_y = \rho v$. The IDO-CF scheme in two-dimension defines the cell-integrated (surface-integrated) value ${}^{xy}\mathbf{Q}_{i,j} \equiv \int_{y_{j-1/2}}^{y_{j+1/2}} \int_{x_{i-1/2}}^{x_{i+1/2}} \mathbf{Q}\,dx\,dy$, the line-integrated values ${}^{x}\mathbf{Q}_{i,j+1/2} \equiv \int_{x_{j-1/2}}^{x_{i+1/2}} \mathbf{Q}\,dx$, ${}^{y}\mathbf{Q}_{i+1/2,j} \equiv \int_{y_{j-1/2}}^{y_{j+1/2}} \mathbf{Q}\,dy$, and the point value $\mathbf{Q}_{i+1/2,j+1/2}$ as time-integrated variables. Fig. 1 shows the configuration of these values. We solve the following equations derived from Eq. (40):

$$ \frac{\partial}{\partial t}\, {}^{xy}\mathbf{Q}_{i,j} = -{}^{y}\mathbf{E}_{i+1/2,j} + {}^{y}\mathbf{E}_{i-1/2,j} - {}^{x}\mathbf{F}_{i,j+1/2} + {}^{x}\mathbf{F}_{i,j-1/2}, \tag{41} $$

$$ \frac{\partial}{\partial t}\, {}^{x}\mathbf{Q}_{i,j+1/2} = -\mathbf{E}_{i+1/2,j} + \mathbf{E}_{i-1/2,j} - {}^{x}\frac{\partial \mathbf{F}}{\partial y}_{i,j+1/2}, \tag{42} $$

$$ \frac{\partial}{\partial t}\, {}^{y}\mathbf{Q}_{i+1/2,j} = -{}^{y}\frac{\partial \mathbf{E}}{\partial x}_{i+1/2,j} - \mathbf{F}_{i,j+1/2} + \mathbf{F}_{i,j-1/2}, \tag{43} $$

$$ \frac{\partial}{\partial t}\, \mathbf{Q}_{i+1/2,j+1/2} = -\frac{\partial \mathbf{E}}{\partial x}_{i+1/2,j+1/2} - \frac{\partial \mathbf{F}}{\partial y}_{i+1/2,j+1/2}. \tag{44} $$

Most terms in the above equations can be discretized using the same procedure with that of the one-dimensional Euler equations. In contrast to the one-dimensional case, the line integrals of the fluxes including nonlinear terms as ϕu appear in Eq. (41), for example, the first term of the right hand side is

$$ {}^{y}\mathbf{E}_{i+1/2,j} = \begin{bmatrix} {}^{y}(\rho u)^{\mathrm{LI}}_{i+1/2,j} \\ {}^{y}(m_x u)^{\mathrm{LI}}_{i+1/2,j} + {}^{y}p_{i+1/2,j} \\ {}^{y}(m_y u)^{\mathrm{LI}}_{i+1/2,j} \\ {}^{y}(eu)^{\mathrm{LI}}_{i+1/2,j} + {}^{y}(pu)^{\mathrm{LI}}_{i+1/2,j} \end{bmatrix}, \tag{45} $$

where the superscript LI represents the line integral approximation. For high-order approximation of such nonlinear terms, we use the interpolation function (24), and the line integral of the nonlinear term can be expressed as

$$ {}^{y}(\phi u)^{\mathrm{LI}}_{j} = \int_0^h \Phi^{\mathrm{IN}}(Y) U^{\mathrm{IN}}(Y)\mathrm{d}Y. \tag{46} $$

The line integral has fifth-order accuracy (see Appendix 5). The expression can be simplified as a matrix form:

$$ {}^{y}(\phi u)^{\mathrm{LI}}_{j} = \begin{pmatrix} \phi_{j-1/2} & \frac{{}^{y}\phi_j}{h} & \phi_{j+1/2} \end{pmatrix} \mathbf{\Omega} \begin{pmatrix} u_{j-1/2} \\ {}^{y}u_j/h \\ u_{j+1/2} \end{pmatrix}, \tag{47} $$

where

$$ \mathbf{\Omega} = \frac{h}{30} \begin{pmatrix} 4 & -3 & -1 \\ -3 & 36 & -3 \\ -1 & -3 & 4 \end{pmatrix}. $$

Eqs. (42) and (43) also involve the line-integral of nonlinear terms ${}^{x}(\partial\phi v/\partial y) = {}^{x}(v\partial\phi/\partial y + \phi\partial v/\partial y)$ as

$$ {}^{x}\frac{\partial \mathbf{F}}{\partial y}_{i,j+1/2} = \begin{bmatrix} {}^{x}\frac{\partial \rho v}{\partial y}^{\mathrm{LI}}_{i,j+1/2} \\ {}^{x}\frac{\partial m_x v}{\partial y}^{\mathrm{LI}}_{i,j+1/2} \\ {}^{x}\frac{\partial m_y v}{\partial y}^{\mathrm{LI}}_{i,j+1/2} + \frac{\partial ({}^{x}p)}{\partial y}^{\mathrm{C}}_{i,j+1/2} \\ {}^{x}\frac{\partial e v}{\partial y}^{\mathrm{LI}}_{i,j+1/2} + {}^{x}\frac{\partial p v}{\partial y}^{\mathrm{LI}}_{i,j+1/2} \end{bmatrix} = \begin{bmatrix} {}^{x}\left(\rho\frac{\partial v}{\partial y} + v\frac{\partial \rho}{\partial y}\right)^{\mathrm{LI}}_{i,j+1/2} \\ {}^{x}\left(m_x\frac{\partial v}{\partial y} + v\frac{\partial m_x}{\partial y}\right)^{\mathrm{LI}}_{i,j+1/2} \\ {}^{x}\left(m_y\frac{\partial v}{\partial y} + v\frac{\partial v}{\partial y}\right)^{\mathrm{LI}}_{i,j+1/2} + \frac{\partial ({}^{x}p)}{\partial y}^{\mathrm{C}}_{i,j+1/2} \\ {}^{x}\left(e\frac{\partial v}{\partial y} + v\frac{\partial e}{\partial y}\right)^{\mathrm{LI}}_{i,j+1/2} + {}^{x}\left(p\frac{\partial v}{\partial y} + v\frac{\partial p}{\partial y}\right)^{\mathrm{LI}}_{i,j+1/2} \end{bmatrix}. \tag{48} $$

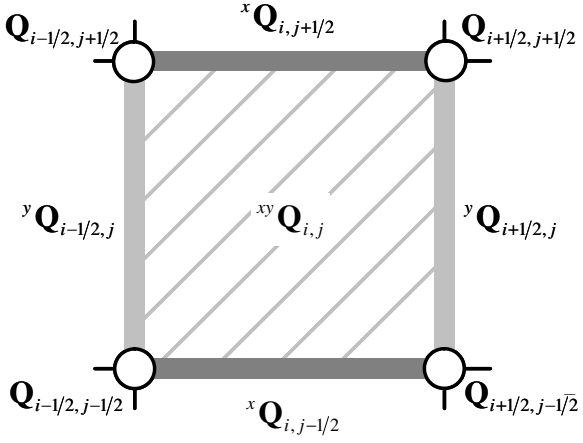

Fig. 1. Configuration of time-integrated variables.

The approximation procedure of the terms is divided into two steps. First, we calculate the line-integrated values ${}^x(\partial\phi/\partial y)_i$ and ${}^x(\partial v/\partial y)_i$, and the point values $\partial\phi/\partial y_{i\pm1/2}$ and $\partial v/\partial y_{i\pm1/2}$. We apply the upwind discretization to ${}^x(\partial\phi/\partial y)_i$ and $\partial\phi/\partial y_{i\pm1/2}$, and the central discretization to ${}^x(\partial v/\partial y)_i$ and $\partial v/\partial y_{i\pm1/2}$, where we regard ${}^x(\partial\phi/\partial y)_i$ as the derivative of ${}^x\phi$, e.g.

$$\left.\frac{\partial({}^x\phi)^{\mathrm{UP}}}{\partial y}\right|_{i,j+1/2} = \frac{6}{h^2}\,{}^{xy}\phi_{i,j+1} - \frac{2}{h}({}^x\phi_{i,j+3/2} + 2\,{}^x\phi_{i,j+1/2}). \tag{49}$$

Then, applying Eq. (47) to these values, we obtain the line-integral as

$${}^x\left(\frac{\partial\phi v}{\partial y}\right)_i^{\mathrm{LI}} = {}^x\left(\phi\frac{\partial v}{\partial y}\right)_i^{\mathrm{LI}} + {}^x\left(v\frac{\partial\phi}{\partial y}\right)_i^{\mathrm{LI}}, \tag{50}$$

where

$${}^x\left(\phi\frac{\partial v}{\partial y}\right)_i^{\mathrm{LI}} = \begin{pmatrix}\phi_{i-1/2} & \frac{{}^x\phi_i}{h} & \phi_{i+1/2}\end{pmatrix}\mathbf{\Omega}\begin{pmatrix}\frac{\partial v}{\partial y}^{\mathrm{C}}_{i-1/2}\\ {}^x\frac{\partial v}{\partial y}^{\mathrm{C}}_i/h\\ \frac{\partial v}{\partial y}^{\mathrm{C}}_{i+1/2}\end{pmatrix}$$

and

$${}^x\left(v\frac{\partial\phi}{\partial y}\right)_i^{\mathrm{LI}} = \begin{pmatrix}v_{i-1/2} & \frac{{}^xv_i}{h} & v_{i+1/2}\end{pmatrix}\mathbf{\Omega}\begin{pmatrix}\frac{\partial\phi}{\partial y}^{\mathrm{UP}}_{i-1/2}\\ {}^x\frac{\partial\phi}{\partial y}^{\mathrm{UP}}_i/h\\ \frac{\partial\phi}{\partial y}^{\mathrm{UP}}_{i+1/2}\end{pmatrix}.$$

In the previous section, we have shown the approximations of the point values and the line-integrated values of primitive variables. In calculating the surface-integrated values of primitive variables, the Simpson integration is introduced such as

$${}^{xy}u_{i,j} = \frac{h}{6}({}^xu_{i,j+1/2} + 4\,{}^xu_{i,jc} + {}^xu_{i,j-1/2}), \tag{51}$$

where the line-integrated values in Eq. (51) can be obtained from Eq. (29).

2.5. Incompressible flow

The governing equations for two-dimensional incompressible Newtonian fluid are described as the following divergence free condition and Navier–Stokes equation:

$$\frac{\partial u}{\partial x} + \frac{\partial v}{\partial y} = 0, \tag{52}$$

$$\frac{\partial\mathbf{u}}{\partial t} = -\frac{\partial\mathbf{E}}{\partial x} - \frac{\partial\mathbf{F}}{\partial y},$$

$$\mathbf{u} = \begin{bmatrix}u\\ v\end{bmatrix}, \quad \mathbf{E} = \begin{bmatrix}u^2 + p - \frac{1}{Re}\frac{\partial u}{\partial x}\\ uv - \frac{1}{Re}\frac{\partial v}{\partial x}\end{bmatrix}, \quad \mathbf{F} = \begin{bmatrix}uv - \frac{1}{Re}\frac{\partial u}{\partial y}\\ v^2 + p - \frac{1}{Re}\frac{\partial v}{\partial y}\end{bmatrix}. \tag{53}$$

The divergence of Eq. (53) should be satisfied with the divergence free condition:

$$\nabla\cdot\frac{\partial\mathbf{u}}{\partial t} = \frac{\partial}{\partial t}(\nabla\cdot\mathbf{u}) = 0. \tag{54}$$

We apply a semi-implicit procedure like Simplified Marker-And-Cell (SMAC) method [23,24] to the solution of the Navier–Stokes equation. First, we calculate pseudo-time derivatives relating to advection and viscous terms with the similar way to the Euler equations:

$$\frac{\partial}{\partial t}{}^{xy}\mathbf{u}^*_{i,j} = -{}^{y}\mathbf{E}^*_{i+1/2,j} + {}^{y}\mathbf{E}^*_{i-1/2,j} - {}^{x}\mathbf{F}^*_{i,j+1/2} + {}^{x}\mathbf{F}^*_{i,j-1/2}, \tag{55}$$

$$\frac{\partial}{\partial t}{}^{x}\mathbf{u}^*_{i,j+1/2} = -\mathbf{E}^*_{i+1/2,j} + \mathbf{E}^*_{i-1/2,j} - {}^{x}\frac{\partial \mathbf{F}^*}{\partial y}_{i,j+1/2}, \tag{56}$$

$$\frac{\partial}{\partial t}{}^{y}\mathbf{u}^*_{i+1/2,j} = -{}^{y}\frac{\partial \mathbf{E}^*}{\partial x}_{i+1/2,j} - \mathbf{F}^*_{i,j+1/2} + \mathbf{F}^*_{i,j-1/2}, \tag{57}$$

$$\frac{\partial}{\partial t}\mathbf{u}^*_{i+1/2,j+1/2} = -\frac{\partial \mathbf{E}^*}{\partial x}_{i+1/2,j+1/2} - \frac{\partial \mathbf{F}^*}{\partial y}_{i+1/2,j+1/2}, \tag{58}$$

where

$$\mathbf{E}^* = \begin{bmatrix} u^2 - \frac{1}{Re}\frac{\partial u}{\partial x} \\ uv - \frac{1}{Re}\frac{\partial v}{\partial x} \end{bmatrix}, \quad \mathbf{F}^* = \begin{bmatrix} uv - \frac{1}{Re}\frac{\partial u}{\partial y} \\ v^2 - \frac{1}{Re}\frac{\partial v}{\partial y} \end{bmatrix},$$

and the viscous terms are discretized by using the central discretizations. The pressure Poisson equation is derived from Eq. (54):

$$\nabla \cdot \frac{\partial \mathbf{u}}{\partial t} = \nabla \cdot \frac{\partial \mathbf{u}^*}{\partial t} - \nabla \cdot (\nabla p) = 0. \tag{59}$$

The integral operation to Eq. (59) makes the following coupled equations for the cell-integrated, line-integrated, and point values:

$$\frac{\partial ({}^{y}p)^{\mathrm{C}}}{\partial x}_{i+1/2,j} - \frac{\partial ({}^{y}p)^{\mathrm{C}}}{\partial x}_{i-1/2,j} + \frac{\partial ({}^{x}p)^{\mathrm{C}}}{\partial y}_{i,j+1/2} - \frac{\partial ({}^{x}p)^{\mathrm{C}}}{\partial y}_{i,j-1/2} = {}^{xy}s_{i,j}, \tag{60}$$

$$\frac{\partial p^{\mathrm{C}}}{\partial x}_{i+1/2,j+1/2} - \frac{\partial p^{\mathrm{C}}}{\partial x}_{i-1/2,j+1/2} + \frac{\partial^2 ({}^{x}p)^{\mathrm{C}}}{\partial y^2}_{i,j+1/2} = {}^{x}s_{i,j+1/2}, \tag{61}$$

$$\frac{\partial^2 ({}^{y}p)^{\mathrm{C}}}{\partial x^2}_{i+1/2,j} + \frac{\partial p^{\mathrm{C}}}{\partial y}_{i+1/2,j+1/2} - \frac{\partial p^{\mathrm{C}}}{\partial y}_{i+1/2,j-1/2} = {}^{y}s_{i+1/2,j}, \tag{62}$$

$$\frac{\partial^2 p^{\mathrm{C}}}{\partial x^2}_{i+1/2,j+1/2} + \frac{\partial^2 p^{\mathrm{C}}}{\partial y^2}_{i+1/2,j+1/2} = s_{i+1/2,j+1/2}. \tag{63}$$

The source terms ${}^{xy}s_{i,j}$, ${}^{x}s_{i,j+1/2}$, ${}^{y}s_{i+1/2,j}$, and $s_{i+1/2,j+1/2}$ are

$${}^{xy}s_{i,j} = \frac{\partial}{\partial t}{}^{y}u^*_{i+1/2,j} - \frac{\partial}{\partial t}{}^{y}u^*_{i-1/2,j} + \frac{\partial}{\partial t}{}^{x}v^*_{i,j+1/2} - \frac{\partial}{\partial t}{}^{x}v^*_{i,j-1/2}, \tag{64}$$

$${}^{x}s_{i,j+1/2} = \frac{\partial u^*}{\partial t}_{i+1/2,j+1/2} - \frac{\partial u^*}{\partial t}_{i-1/2,j+1/2} + \frac{\partial}{\partial y}\left(\frac{\partial}{\partial t}{}^{x}v^*\right)^{\mathrm{C}}_{i,j+1/2}, \tag{65}$$

$${}^{y}s_{i+1/2,j} = \frac{\partial}{\partial x}\left(\frac{\partial}{\partial t}{}^{y}u^*\right)^{\mathrm{C}}_{i+1/2,j} + \frac{\partial v^*}{\partial t}_{i+1/2,j+1/2} - \frac{\partial v^*}{\partial t}_{i+1/2,j-1/2}, \tag{66}$$

$$s_{i+1/2,j+1/2} = \frac{\partial}{\partial x}\left(\frac{\partial u^*}{\partial t}\right)^{\mathrm{C}}_{i+1/2,j+1/2} + \frac{\partial}{\partial y}\left(\frac{\partial v^*}{\partial t}\right)^{\mathrm{C}}_{i+1/2,j+1/2}. \tag{67}$$

These source terms are estimated by the pseudo-time derivatives. Eqs. (60)–(63) can be solved by using iteration methods such as SOR, BiCGStab [25], and the pressure field is obtained. Adding the pressure gradient terms to the pseudo-time derivatives, we have the correct time derivatives with the divergence free, for example,

$$\frac{\partial}{\partial t}{}^{xy}u_{i,j} = \frac{\partial}{\partial t}{}^{xy}u^*_{i,j} - {}^{y}p_{i+1/2,j} + {}^{y}p_{i-1/2,j}, \tag{68}$$

$$\frac{\partial}{\partial t}{}^{x}u_{i,j+1/2} = \frac{\partial}{\partial t}{}^{x}u^*_{i,j+1/2} - p_{i+1/2,j+1/2} + p_{i-1/2,j+1/2}, \tag{69}$$

$$\frac{\partial}{\partial t}{}^{y}u_{i+1/2,j} = \frac{\partial}{\partial t}{}^{y}u^{*}_{i+1/2,j} - \frac{\partial({}^{y}p)^{\mathrm{C}}}{\partial x}_{i+1/2,j}, \tag{70}$$

$$\frac{\partial}{\partial t}u_{i+1/2,j+1/2} = \frac{\partial}{\partial t}u^{*}_{i+1/2,j+1/2} - \frac{\partial p^{\mathrm{C}}}{\partial x_{i+1/2,j+1/2}}. \tag{71}$$

It is found that the Navier–Stokes equation can be reduced to a complete divergence free form for the cell. The velocity field in each stage of Runge–Kutta time integration can be satisfied with the divergence free condition.

2.6. Velocity–pressure coupling

Numerical coupling between velocity field and pressure field is an important issue in numerical schemes. Since the collocated configuration of velocity and pressure (collocated grids) generally shows low numerical coupling, staggered grids or special discretizations are often applied. In the non-conservative form of the IDO (IDO-NCF) scheme, we use special discretizations called stable coupling method for computations on collocated grids [13]. In the IDO-CF scheme, both the compressible and incompressible fluid equations are solved on collocated grids for velocity and pressure, where their cell-integrated values and point values have a staggered configuration as shown in Fig. 1. The configuration guarantees tight coupling between velocity and pressure without any stable coupling methods as used in the IDO-NCF scheme.

3. Fourier analysis

In the paper [12], we presented the Fourier analysis method for the IDO-NCF scheme to evaluate stability and accuracy in solving linear partial differential equations. The method is also applicable to the IDO-CF scheme. This section provides the stability and the accuracy for solutions of advection, diffusion, and Poisson equations.

3.1. Advection equation

The one-dimensional advection equation with the constant velocity u is considered:

$$\frac{\partial \phi}{\partial t} = -\frac{\partial}{\partial x}(u\phi). \tag{72}$$

When the spatial profile of a dependent variable $\phi(x)$ is assumed to be periodic over the domain $[0, L]$ with uniform grid spacing $h = L/N$, the dependent variable is decomposed into Fourier series,

$$\phi(x) = \sum_{k} \hat{\phi}(k)\mathrm{e}^{\mathrm{i}wx/h}, \tag{73}$$

where $\mathrm{i} = \sqrt{-1}$, and $w = 2\pi kh/L$ is a scaled wavenumber. The integrated value of the dependent variable is also decomposed as

$$\int \phi(x)\mathrm{d}x = \sum_{k} {}^{x}\hat{\phi}(k)\mathrm{e}^{\mathrm{i}wx/h}. \tag{74}$$

Using the same procedure in [12], we can describe the time integration in the following matrix form:

$$\begin{pmatrix} {}^{x}\hat{\phi}(k)^{n+1} \\ \hat{\phi}(k)^{n+1} \end{pmatrix} = \mathbf{S}\begin{pmatrix} {}^{x}\hat{\phi}(k)^{n} \\ \hat{\phi}(k)^{n} \end{pmatrix} = \mathbf{L}\begin{pmatrix} \lambda^{+} & 0 \\ 0 & \lambda^{-} \end{pmatrix}^{n}\mathbf{L}^{-1}\begin{pmatrix} {}^{x}\hat{\phi}(k)^{0} \\ \hat{\phi}(k)^{0} \end{pmatrix}, \tag{75}$$

where $\mathbf{L} = \begin{pmatrix} \mathbf{K}^{+} & \mathbf{K}^{-} \end{pmatrix}$, $\mathbf{L}\mathbf{L}^{-1} = \mathbf{I}$, and $\lambda^{\pm}$ and $\mathbf{K}^{\pm}$ are eigenvalues and eigenvectors of $\mathbf{S}$. The matrix $\mathbf{S}$ is exactly same with that of the IDO-NCF scheme. The stability condition requires the absolute values of the eigenvalues are less than unity for all the wavenumbers. Figs. 2 and 3 show the Courant number limitation related to the stability condition for the central discretization and the upwind discretization, respectively. The Courant number is determined by $C = |u|\Delta t/h$. First-order Runge–Kutta time integration is absolutely unstable for

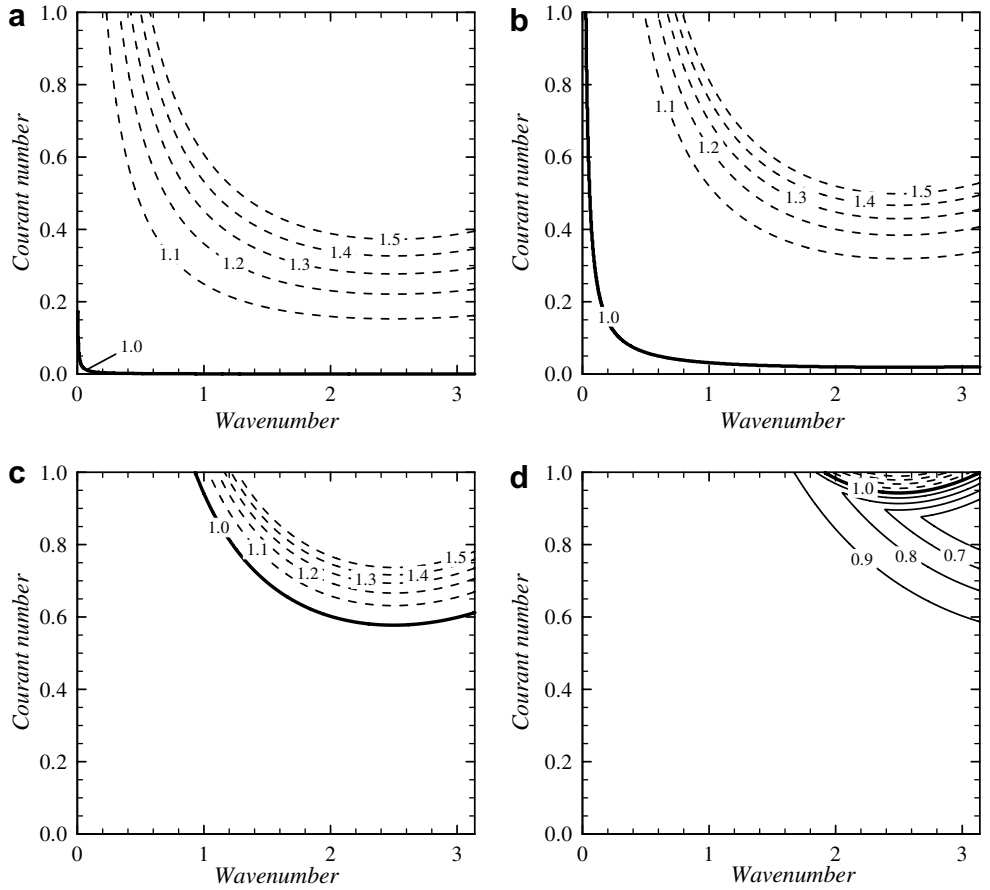

Fig. 2. Contour plots of eigenvalues for time integration of advection equation by central discretization: (a) first-order Runge–Kutta; (b) second-order Runge–Kutta; (c) third-order Runge–Kutta; and (d) fourth-order Runge–Kutta.

both the discretizations. Higher-order Runge–Kutta method enlarges Courant number limitation, and the maximum Courant number is defined as 0.86 for the central discretization with the fourth-order Runge–Kutta method, and that of the upwind discretization is 0.42. Numerical phase for the advection calculation is presented in Fig. 4a. As references, the phases of the fourth-order CD scheme and the sixth-order combined compact difference (CCD) scheme [26] are also shown. The IDO-CF scheme provides accurate phase for a wide range of wavenumbers in comparison with the CD and CCD schemes. Numerical gain shown in Fig. 4b presents that the central discretization has no numerical dissipation and the upwind discretization gives less dissipative solutions than the third-order upwind finite difference (FD) scheme. As illustrated in Fig. 5, the phase errors of both the central and upwind discretizations, and also the gain errors of the upwind discretization have fourth-order convergence.

3.2. Diffusion equation

We examine the solution of the one-dimensional diffusion equation:

$$\frac{\partial \phi}{\partial t} = -\frac{\partial}{\partial x}\left(-\mu \frac{\partial \phi}{\partial x}\right), \tag{76}$$

where the diffusion coefficient μ is a constant. For the time integration of the equation given by Eq. (75), the eigenvalues of the diffusion equation are plotted in Fig. 6, where the diffusion number is $D = \mu \Delta t / h^2$. The use

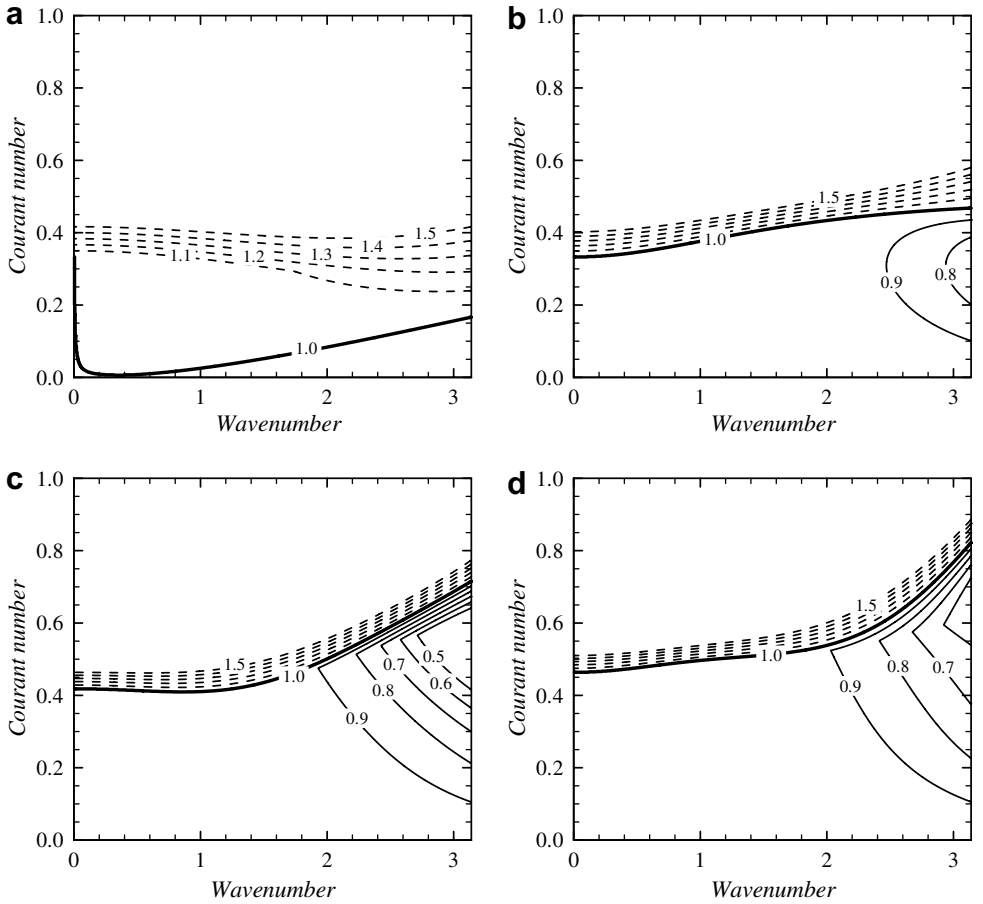

Fig. 3. Contour plots of eigenvalues for time integration of advection equation by upwind discretization: (a) first-order Runge–Kutta; (b) second-order Runge–Kutta; (c) third-order Runge–Kutta; and (d) fourth-order Runge–Kutta.

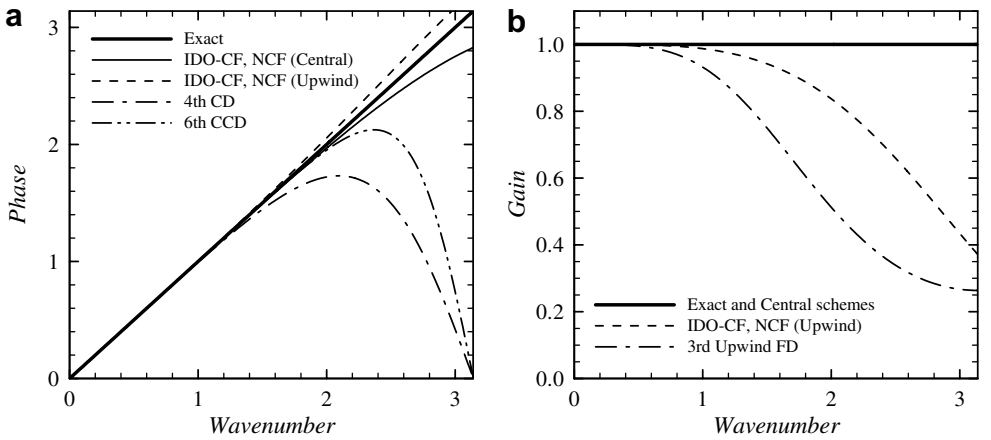

Fig. 4. Results of Fourier analysis for advection equation: (a) phase and (b) gain.

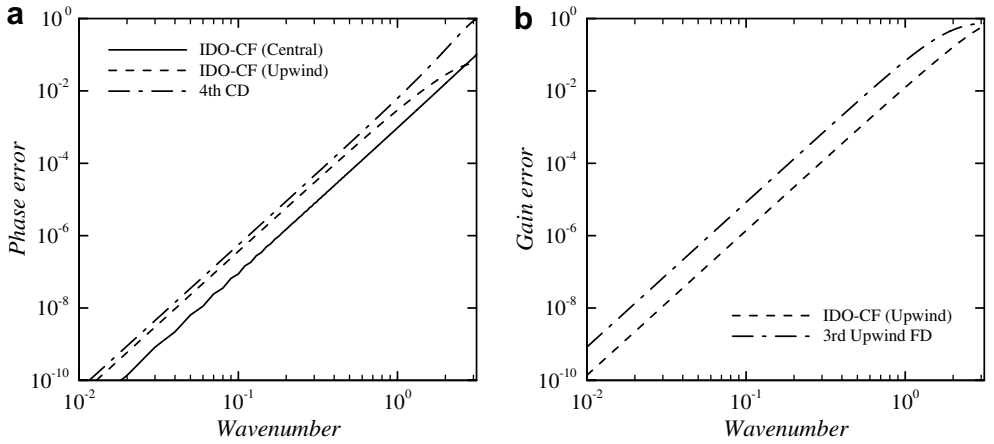

Fig. 5. Numerical errors for advection equation: (a) phase error and (b) gain error.

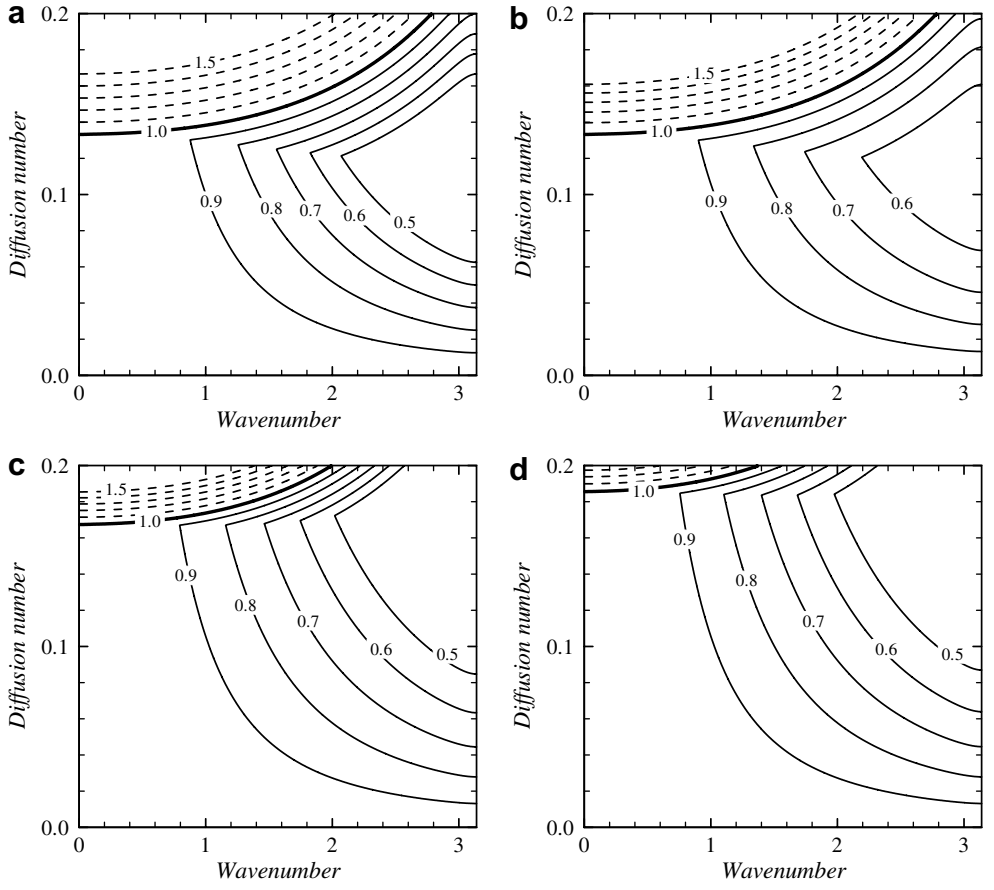

Fig. 6. Contour plots of eigenvalues for time integration of diffusion equation: (a) first-order Runge–Kutta; (b) second-order Runge–Kutta; (c) third-order Runge–Kutta; and (d) fourth-order Runge–Kutta.

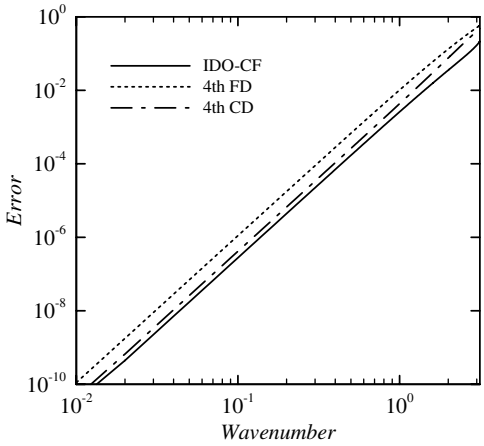

Fig. 7. Numerical errors for diffusion equation.

of high-order Runge–Kutta method increases diffusion number limit. For the fourth-order Runge–Kutta method, we can define the maximum diffusion number as 0.18. Fig. 7 shows the numerical errors. The IDO-CF scheme has fourth-order accuracy and the errors are less than other fourth-order schemes for all the wavenumbers.

3.3. Poisson equation

Poisson equation for pressure field has an important role in solving incompressible fluid equations. The following one-dimensional Poisson equation is considered:

$$-\frac{\partial}{\partial x}\left(-\frac{\partial \phi}{\partial x}\right) = s, \tag{77}$$

where s is the source term. The solution of the Poisson equation is expressed as

$${}^{x}\hat{\phi}^{n}(k) = T(w)\,{}^{x}\hat{\phi}(k), \tag{78}$$

where the function $T(w)$ is the transfer function, representing the ratio of the numerical solution to the exact solution. The transfer function of the IDO-CF scheme follows the exact solution more closely than other schemes. The errors of the Poisson equation also have fourth-order convergence as shown in Fig. 8.

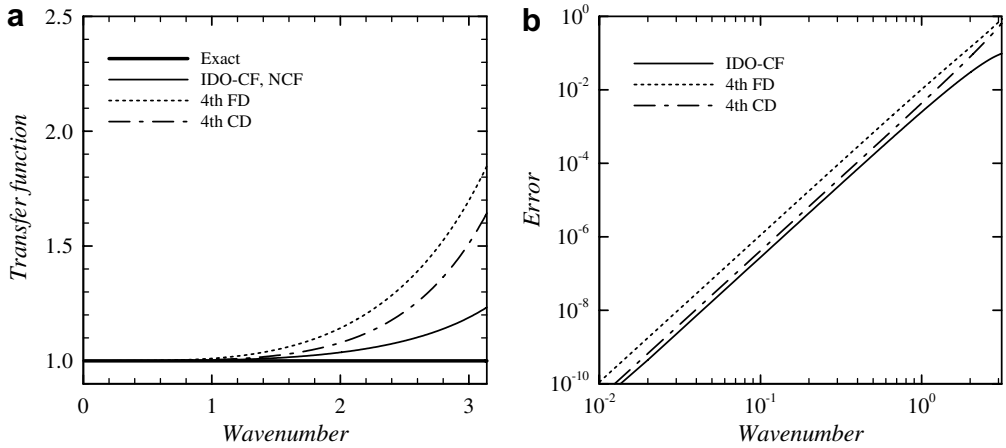

Fig. 8. Fourier analysis of Poisson equation: (a) transfer function and (b) error.

4. Numerical results

4.1. One-dimensional Riemann problem

As is commonly used, we examine the one-dimensional Riemann problem by Sod [27]. The initial conditions for this problem are given by the following primitive variables:

$$(\rho \quad u \quad p) = \begin{cases} (1.0 \quad 0.0 \quad 1.0) & \text{for } x \leqslant 1.0 \\ (0.125 \quad 0.0 \quad 0.1) & \text{for } x > 1.0 \end{cases}. \tag{79}$$

The fluid is assumed to be ideal gas, and the specific heat ratio is $\gamma = 1.4$. In this computation, we add an artificial viscosity described in Appendix 6 to the compressed region. Fig. 9 illustrates computed density and pressure profiles at $t = 0.5$ with exact solutions, where the cell size is $h = 1/100$ and the Courant number is $|u|\Delta t/h = 0.3$. Both the density and pressure profiles are consistent with those of the exact solutions. Fig. 10a shows the magnified view of the density profile around the contact discontinuity. Small overshooting and undershooting are observed at the contact discontinuity. In order to remove the non-physical oscillations, such monotone functions as a rational function proposed by Xiao et al. [28] are applicable to the discretizations of advection terms. In Fig. 10b, we present the computed density profile by the IDO-CF scheme with the

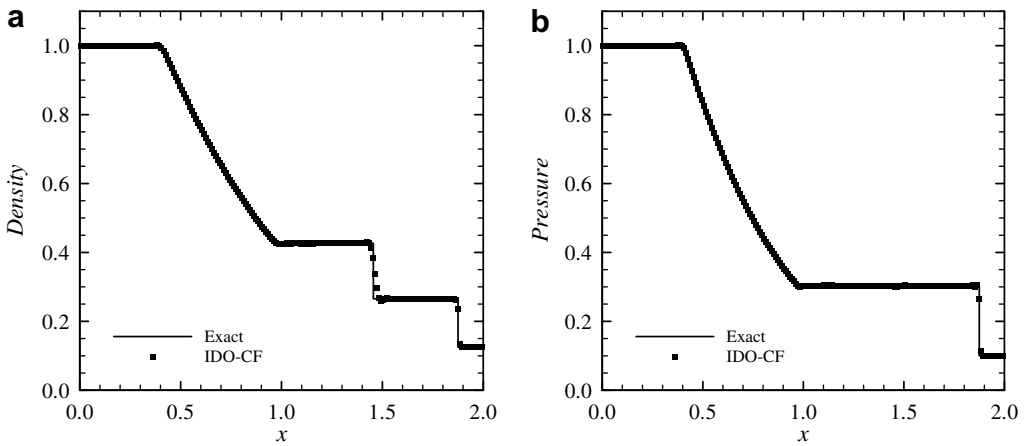

Fig. 9. Numerical result of the one-dimensional Riemann problem: (a) density and (b) pressure.

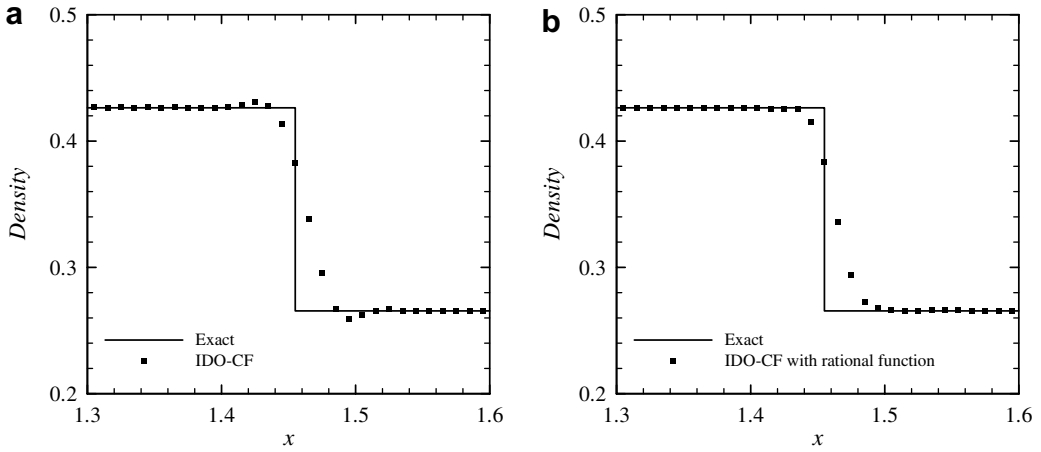

Fig. 10. Density profile around the contact interface: (a) IDO-CF and (b) IDO-CF with rational function.

rational function. It is found that the density profile has no oscillation at the contact discontinuity, while the profile in the other region has consistency with the exact profile.

4.2. Two-dimensional Riemann problem

Two-dimensional Riemann problems proposed in [29] are used to demonstrate the estimation for multi-dimensional compressible fluid dynamics. Square computational domain $[0,1]\times[0,1]$ is initially divided into four quadrants, where each quadrant has different initial states $(\rho_l \quad u_l \quad v_l \quad p_l)$ as illustrated in Fig. 11a. The initial states are set so that only a forward shock wave $\vec{S}_{lr}$, a backward shock wave $\overleftarrow{S}_{lr}$, a forward rarefaction wave $\vec{R}_{lr}$, a backward rarefaction wave $\overleftarrow{R}_{lr}$, a negative contact discontinuity J^-_{lr} or a positive constant discontinuity J^+_{lr} connects two neighboring states. The fluid is assumed to be ideal gas with the specific heat ratio $\gamma = 1.4$. Fig. 11b shows the density contours at $\underleftarrow{t} = 0.25$ for Configuration D in Ref. [29], where the rarefaction and the contact discontinuities are interacted: $\vec{R}_{21}J^-_{32}J^-_{34}\overleftarrow{R}_{41}$. The initial conditions are given by

Configuration D:

$$(\rho_l \quad u_l \quad v_l \quad p_l) = \begin{cases} (0.5197 & 0.1 & 0.1 & 0.4) & \text{for } l = 1 \\ (1.0 & -0.6259 & 0.1 & 1.0) & \text{for } l = 2 \\ (0.8 & 0.1 & 0.1 & 1.0) & \text{for } l = 3 \\ (1.0 & 0.1 & -0.6259 & 1.0) & \text{for } l = 4 \end{cases}. \tag{80}$$

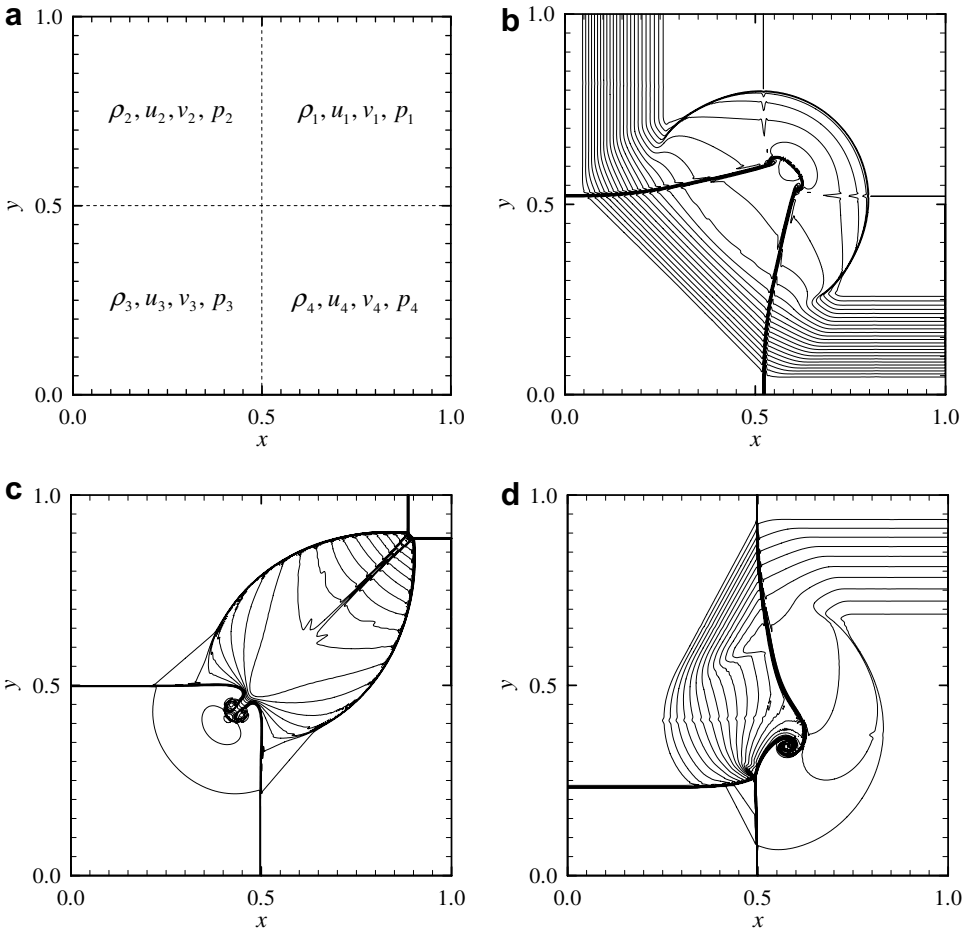

Fig. 11. Density contours in two-dimensional Riemann problems: (a) initial state; (b) Configuration D; (c) Configuration F; and (d) Configuration K in [29].

The Courant number is $|\mathbf{u}|\Delta t/h = 0.2$. In order to compare with the references, we use 400×400 cells in this computation. Both the discontinuities and a circular shock wave are described sharper than those obtained from other high resolution schemes [29–32]. Fig. 11c and d shows numerical results of other configurations, Configuration F: $\vec{S}_{21}J^{+}_{32}J^{+}_{34}\vec{S}_{41}$ at $t = 0.25$, and Configuration K: $J^{+}_{21}\vec{S}_{32}J^{-}_{34}\vec{R}_{41}$ at $t = 0.3$ in [29], where the initial conditions are

Configuration F:

$$(\rho_l \quad u_l \quad v_l \quad p_l) = \begin{cases} (0.5313 & 0.0 & 0.0 & 0.4) & \text{for } l = 1 \\ (1.0 & 0.7276 & 0.0 & 1.0) & \text{for } l = 2 \\ (0.8 & 0.0 & 0.0 & 1.0) & \text{for } l = 3 \\ (1.0 & 0.0 & 0.7276 & 1.0) & \text{for } l = 4 \end{cases}, \tag{81}$$

Configuration K:

$$(\rho_l \quad u_l \quad v_l \quad p_l) = \begin{cases} (1.0 & 0.0 & 0.3 & 1.0) & \text{for } l = 1 \\ (2.0 & 0.0 & -0.3 & 1.0) & \text{for } l = 2 \\ (1.0625 & 0.0 & 0.2145 & 0.4) & \text{for } l = 3 \\ (0.5197 & 0.0 & -0.4259 & 0.4) & \text{for } l = 4 \end{cases}. \tag{82}$$

The Courant numbers are 0.3 and 0.25 for Configuration F and Configuration K, respectively. In also these cases, the IDO-CF scheme provides the solutions with higher resolutions in comparison with the other schemes. In particular, vortex structures are well described.

4.3. DNS of incompressible turbulent flow

DNS of turbulent flow is a suitable problem for checking resolution characteristics of numerical schemes in solving Navier–Stokes equation for incompressible fluid. We have already reported the IDO-NCF scheme has a resolution comparable to that of the spectral method [33] for two-dimensional DNS of homogeneous isotropic turbulence [13]. Here, we examine the same problem with that of [13], and compare the obtained results with those of the IDO-NCF and the spectral method. The computed energy spectrum at eddy turnover time ETT = 1.5 are presented in Fig. 12, where Reynolds number is 10890.8 and 512×512 cells are used. The IDO-CF scheme also retains a resolution comparable to that of the spectral method. Fig. 13 gives the magnified view of the energy spectrum for high wavenumbers and clearly shows the IDO-CF scheme can resolve high wavenumbers superior to that of the IDO-NCF scheme. The IDO-CF scheme accurately estimates the energy spectrum even for over 1300 wavenumbers. As shown in Fig. 14, time evolution of turbulence statistical quantities completely follow the result of the spectral method.

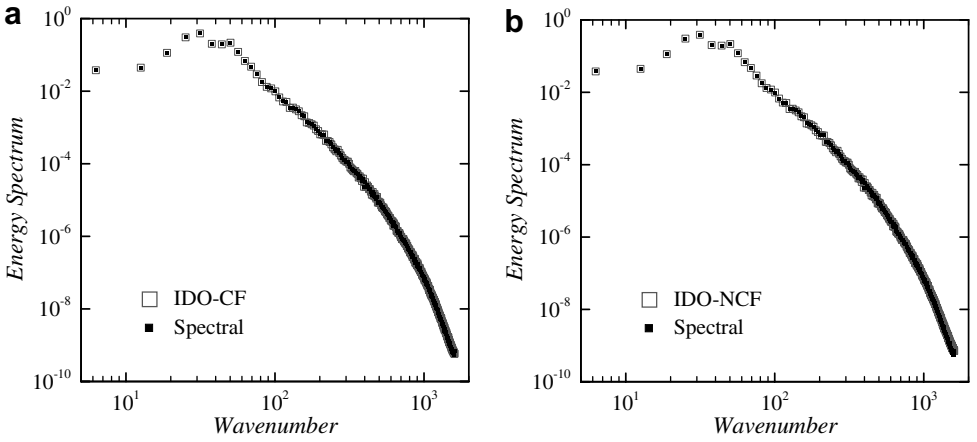

Fig. 12. Energy spectrum for all the wavenumbers at ETT = 1.5: (a) IDO-CF and (b) IDO-NCF.

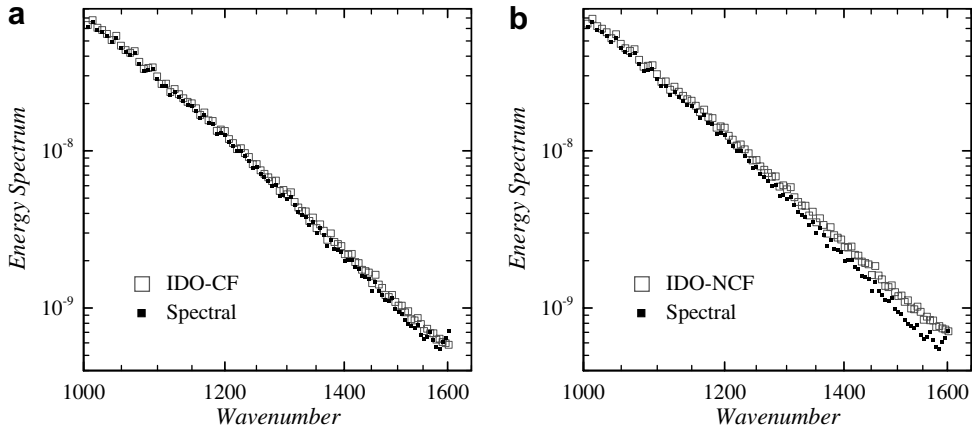

Fig. 13. Energy spectrum for high wavenumbers at ETT = 1.5: (a) IDO-CF and (b) IDO-NCF.

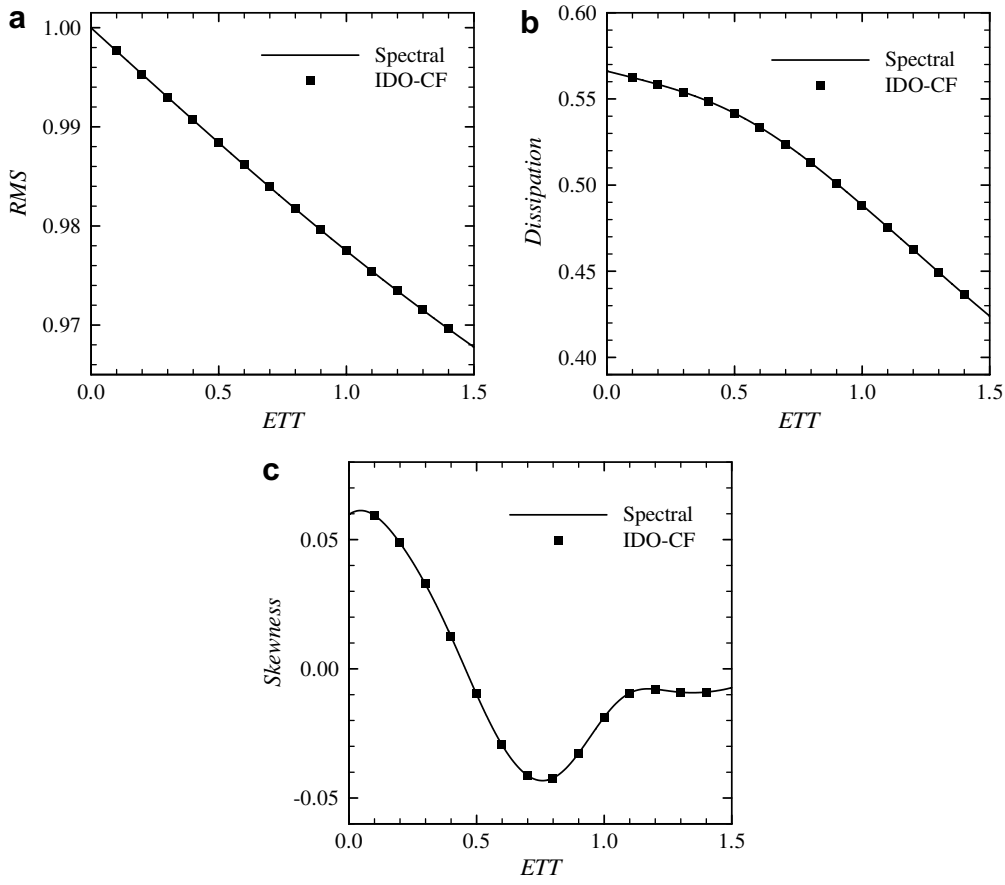

Fig. 14. Time histories of turbulence statistical quantities: (a) root mean square of the velocity; (b) dissipation; and (c) skewness of the x-directional velocity.

4.4. Two-dimensional lid-driven cavity flow

As another benchmark test for incompressible flows, we solve two-dimensional lid-driven cavity flow problems. Fig. 15 shows steady state velocity profiles for Reynolds number 1000, 3200, and 5000. In the

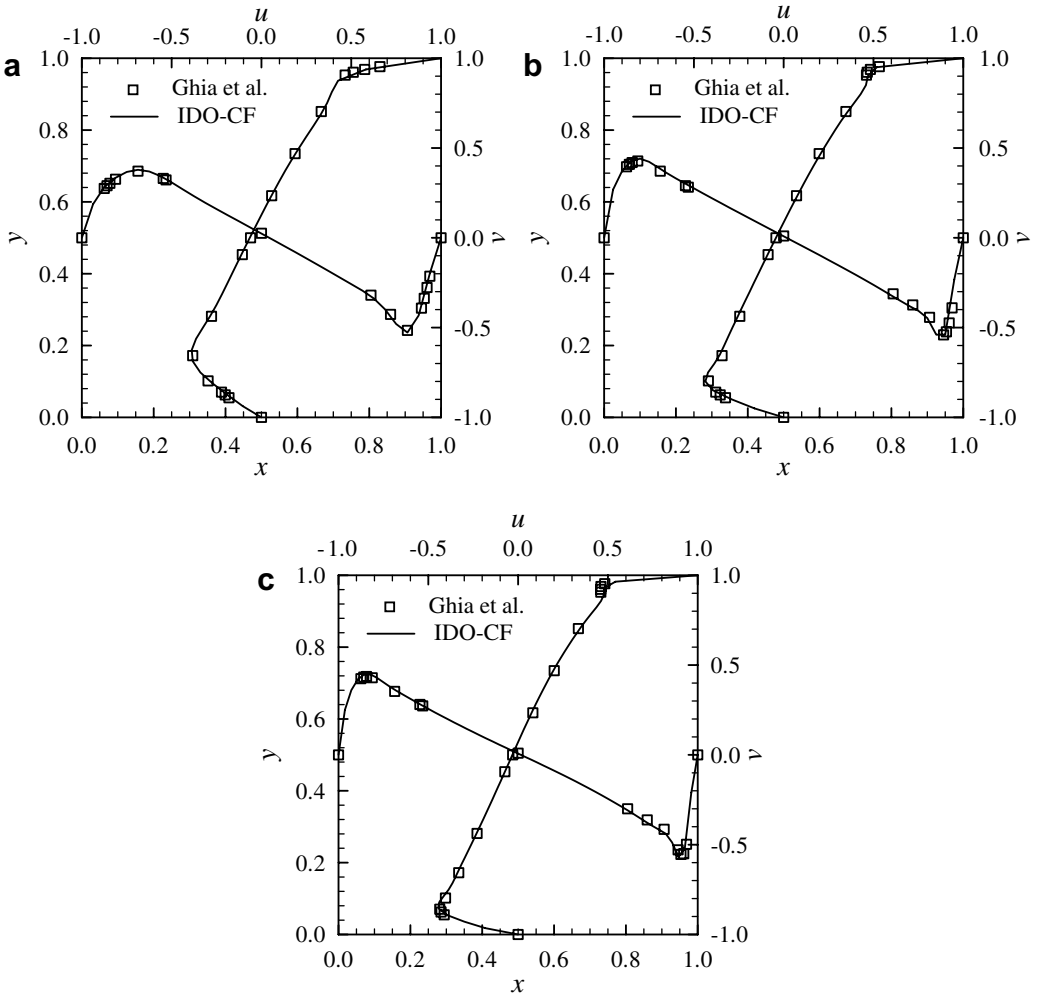

Fig. 15. Numerical results of lid-driven cavity flow: (a) $Re = 1000$ with 32×32 cells; (b) $Re = 3200$ with 40×40 cells; and (c) $Re = 5000$ with 56×56 cells.

computations, we use small number of uniform cells: 32×32 cells for $Re = 1000$; 40×40 cells for $Re = 3200$; and 56×56 cells for $Re = 5000$. Despite using such coarse cells, the plots are in good agreement with those presented by Ghia et al. [34], even in the vicinity of the wall.

5. Conclusions

We have presented the conservative form of the IDO (IDO-CF) scheme. In the IDO-CF scheme, cell-integrated values and point values of the mass, the momentum, and the energy are time-integrated by solving coupled conservation equations. The time integration of the cell-integrated values is described in the flux form and the cell-integrated values are exactly conserved. Fourier analyses for advection, diffusion, and Poisson equations show that the IDO-CF scheme retains as high resolution property as the IDO-NCF scheme. The effectiveness of the proposed scheme in solving compressible fluid dynamics is confirmed in the solutions of Riemann problems. The IDO-CF scheme also provides highly resolved solutions for incompressible fluid dynamics as shown in DNS of turbulent flow and lid-driven cavity flow. In comparison with the IDO-NCF scheme, the IDO-CF scheme has advantages not only in conservation but also in numerical velocity–pressure coupling. While the IDO-NCF scheme needs to introduce special discretizations for stable coupling, in the IDO-CF scheme, the automatically staggered configuration between the cell-integrated values and the

point values provides stable coupling without any special discretizations. These advantages lead to superior results for both the compressible and incompressible flow problems. The proposed scheme can extended to the three-dimensional formulation straightforwardly, where volume integrals are introduced as the conservative cell-integrated values. The exactly conservation, high resolution, and high stability features of the IDO-CF scheme immensely promises in advanced compressible and incompressible fluid dynamics studies.

Appendix 1. Truncation error of central discretizations

Using the Taylor series expansion, we can derive the truncation errors of the central discretizations (11)–(14). At a grid point $i+1/2$, the Taylor series of a variable ϕ is described by

$$\phi(x) = \phi(x_{i+1/2}) + \sum_{k=1}^{\infty} \frac{1}{k!} \frac{\partial^k \phi}{\partial x^k}_{x=x_{i+1/2}} (x - x_{i+1/2})^k. \tag{A.1}$$

We consider uniform meshes with the cell size $h = x_{i+1/2} - x_{i-1/2} = x_{i+3/2} - x_{i+1/2}$. The derivatives are derived using the constraints $\phi(x_{i+1/2}) = \phi_{i+1/2}$, $\phi(x_{i-1/2}) = \phi_{i-1/2}$, $\phi(x_{i+3/2}) = \phi_{i+3/2}$, $\int_{x_{i-1/2}}^{x_{i+1/2}} \phi(x)\mathrm{d}x = {}^x\phi_i$, and $\int_{x_{i+1/2}}^{x_{i+3/2}} \phi(x)\mathrm{d}x = {}^x\phi_{i+1/2}$ as

$$\begin{aligned}
\frac{\partial \phi}{\partial x}_{x=x_{i+1/2}} &= \frac{2}{h^2}({}^x\phi_{i+1} - {}^x\phi_i) - \frac{1}{2h}(\phi_{i+3/2} - \phi_{i-1/2}) + \frac{1}{360}\frac{\partial^5 \phi}{\partial x^5} h^4 + \cdots \\
&= \frac{\partial \phi}{\partial x}^{\mathrm{C}}_{i+1/2} + \frac{1}{360}\frac{\partial^5 \phi}{\partial x^5} h^4 + \cdots,
\end{aligned} \tag{A.2}$$

$$\begin{aligned}
\frac{\partial^2 \phi}{\partial x^2}_{x=x_{i+1/2}} &= \frac{15}{2h^3}({}^x\phi_{i+1} + {}^x\phi_i) - \frac{3}{2h^2}(\phi_{i+3/2} + 8\phi_{i+1/2} + \phi_{i-1/2}) + \frac{1}{840}\frac{\partial^6 \phi}{\partial x^6} h^4 + \cdots \\
&= \frac{\partial^2 \phi}{\partial x^2}^{\mathrm{C}}_{i+1/2} + \frac{1}{840}\frac{\partial^6 \phi}{\partial x^6} h^4 + \cdots
\end{aligned} \tag{A.3}$$

$$\begin{aligned}
\frac{\partial^3 \phi}{\partial x^3}_{x=x_{i+1/2}} &= -\frac{12}{h^4}({}^x\phi_{i+1} - {}^x\phi_i) + \frac{6}{h^3}(\phi_{i+3/2} - \phi_{i-1/2}) - \frac{1}{15}\frac{\partial^5 \phi}{\partial x^5} h^2 + \cdots \\
&= \frac{\partial^3 \phi}{\partial x^3}^{\mathrm{C}}_{i+1/2} - \frac{1}{15}\frac{\partial^5 \phi}{\partial x^5} h^2 + \cdots,
\end{aligned} \tag{A.4}$$

$$\begin{aligned}
\frac{\partial^4 \phi}{\partial x^4}_{x=x_{i+1/2}} &= -\frac{90}{h^5}({}^x\phi_{i+1} + {}^x\phi_i) + \frac{30}{h^4}(\phi_{i+3/2} + 4\phi_{i+1/2} + \phi_{i-1/2}) - \frac{1}{21}\frac{\partial^6 \phi}{\partial x^6} h^2 + \cdots \\
&= \frac{\partial^4 \phi}{\partial x^4}^{\mathrm{C}}_{i+1/2} - \frac{1}{21}\frac{\partial^6 \phi}{\partial x^6} h^2 + \cdots.
\end{aligned} \tag{A.5}$$

The first and second derivatives include fourth-order truncation errors, while the third and fourth derivatives have second-order truncation errors.

Appendix 2. Numerical viscosity in upwind discretization

Comparing the upwind discretization with the central discretization, we estimate numerical viscosity included in the upwind discretizations (16) and (18). When the upwind discretization is expressed as

$$\frac{\partial \phi}{\partial x}^{\mathrm{UP}}_{i+1/2} = \sum_{k=1}^{4} \zeta_k \frac{\partial^k \phi}{\partial x^k}^{\mathrm{C}}_{i+1/2} \tag{A.6}$$

the coefficients ζ_k are determined by

$$\begin{pmatrix} \zeta_1 \\ \zeta_2 \\ \zeta_3 \\ \zeta_4 \end{pmatrix} = \begin{pmatrix} 1 \\ 0 \\ -\mathrm{sign}(u)h^2/12 \\ -\mathrm{sign}(u)h^3/30 \end{pmatrix}, \quad \mathrm{sign}(u) = \begin{Bmatrix} 1 & u \geqslant 0 \\ -1 & u < 0 \end{Bmatrix} \tag{A.7}$$

The upwind discretization includes the third and fourth derivatives as numerical viscosity.

Appendix 3. Truncation error of CIP–CSL2 interpolation

The following expression is obtained from the Taylor series:

$$\begin{aligned}\phi(x) &= \left(-6\left(\frac{X}{h}\right)^2 + 6\left(\frac{X}{h}\right)\right)\frac{{}^x\phi_i}{h} + \left(3\left(\frac{X}{h}\right)^2 - 2\left(\frac{X}{h}\right)\right)\phi_{i+1/2} + \left(3\left(\frac{X}{h}\right)^2 - 4\left(\frac{X}{h}\right) + 1\right)\phi_{i-1/2} \\ &\quad + \left(\frac{1}{6}\left(\frac{X}{h}\right)^3 - \frac{1}{4}\left(\frac{X}{h}\right)^2 + \frac{1}{12}\left(\frac{X}{h}\right)\right)\frac{\partial^3\phi}{\partial x^3}h^3 + \left(\frac{1}{24}\left(\frac{X}{h}\right)^4 - \frac{3}{40}\left(\frac{X}{h}\right)^2 + \frac{1}{30}\left(\frac{X}{h}\right)\right)\frac{\partial^4\phi}{\partial x^4}h^4 + \cdots \\ &= \phi^{\mathrm{IN}}(X) + \left(\frac{1}{6}\left(\frac{X}{h}\right)^3 - \frac{1}{4}\left(\frac{X}{h}\right)^2 + \frac{1}{12}\left(\frac{X}{h}\right)\right)\frac{\partial^3\phi}{\partial x^3}h^3 \\ &\quad + \left(\frac{1}{24}\left(\frac{X}{h}\right)^4 - \frac{3}{40}\left(\frac{X}{h}\right)^2 + \frac{1}{30}\left(\frac{X}{h}\right)\right)\frac{\partial^4\phi}{\partial x^4}h^4 + \cdots, \end{aligned} \tag{A.8}$$

where $X = x - x_{i-1/2}$. Here, the interpolated point X can be rewritten by $X = sh$. The interpolation of the CIP–CSL2 scheme (24) is found to include third-order truncation error. At the cell-centered point $X = h/2$, this interpolation leads to fourth-order expression:

$$\phi(x_{ic}) = \frac{3}{2}\frac{{}^x\phi_i}{h} - \frac{1}{4}(\phi_{i+1/2} + \phi_{i-1/2}) + \frac{1}{1920}\frac{\partial^4\phi}{\partial x^4}h^4 + \cdots = \phi_{ic}^{\mathrm{IN}} + \frac{1}{1920}\frac{\partial^4\phi}{\partial x^4}h^4 + \cdots. \tag{A.9}$$

Appendix 4. Order of accuracy of discretization method for primitive variables

The cell-centered values of the density, the momentum, and the total energy are interpolated with fourth-order truncation error by using Eq. (A.9). The cell-centered value of the velocity is also described with fourth-order accuracy:

$$u(x_{ic}) = \frac{m_{ic}^{\mathrm{IN}} + O_m(h^4)}{\rho_{ic}^{\mathrm{IN}} + O_\rho(h^4)} = u_{ic}^{\mathrm{IN}} + O_u(h^4). \tag{A.10}$$

The Simpson integration is a fifth-order expression:

$$\int_{x_{i-1/2}}^{x_{i+1/2}} u(x)\mathrm{d}x = \frac{h}{6}(u(x_{i-1/2}) + 4u(x_{ic}) + u(x_{i+1/2})) + \frac{1}{2880}\frac{\partial^4 u}{\partial x^4}h^5. \tag{A.11}$$

Thus, the velocity is integrated with fifth-order accuracy:

$$\int_{x_{i-1/2}}^{x_{i+1/2}} u(x)\mathrm{d}x = \frac{h}{6}(u_{i-1/2} + 4(u_{ic}^{\mathrm{IN}} + O_u(h^4)) + u_{i+1/2}) + \frac{1}{2880}\frac{\partial^4 u}{\partial x^4}h^5 = {}^x u_i + O'_{x_u}(h^5). \tag{A.12}$$

The truncation error of the pressure depends on the formulation of EOS. In the EOS for ideal gas, $p = \rho(\gamma - 1)\varepsilon$, the cell-centered value of the pressure has fourth-order accuracy:

$$p(x_{ic}) = (\gamma - 1)\rho(x_{ic})\varepsilon(x_{ic}) = (\gamma - 1)(\rho_{ic}^{\mathrm{IN}} + O_\rho(h^4))(\varepsilon_{ic}^{\mathrm{IN}} + O_\varepsilon(h^4)) = (\gamma - 1)\rho_{ic}^{\mathrm{IN}}\varepsilon_{ic}^{\mathrm{IN}} + O_p(h^4), \tag{A.13}$$

where

$$\varepsilon(x_{ic}) = \frac{e_{ic}^{\mathrm{IN}} + O_e(h^4)}{\rho_{ic}^{\mathrm{IN}} + O_\rho(h^4)} - \frac{1}{2}(u_{ic}^{\mathrm{IN}} + O_u(h^4))^2 = \varepsilon_{ic}^{\mathrm{IN}} + O_\varepsilon(h^4). \tag{A.14}$$

Then, the pressure is integrated with fifth-order truncation error.

Appendix 5. Order of accuracy of integration method for nonlinear quantities

Using Eq. (A.8), the integration method (47) for nonlinear quantities can be rewritten by

$$\int_{y_{j-1/2}}^{y_{j+1/2}} \phi(y)u(y)\mathrm{d}y = \begin{pmatrix} \phi_{j-1/2} & \frac{{}^{y}\phi_j}{h} & \phi_{j+1/2} \end{pmatrix} \mathbf{\Omega} \begin{pmatrix} u_{j-1/2} \\ {}^{y}u_j/h \\ u_{j+1/2} \end{pmatrix} + \frac{1}{720}\left((\phi_{j-1/2} - \phi_{j+1/2}) \frac{\partial^3 u}{\partial y^3} + (u_{j-1/2} - u_{j+1/2}) \frac{\partial^3 \phi}{\partial y^3} \right) h^4 \cdots . \tag{A.15}$$

Since $\phi_{j-1/2} - \phi_{j+1/2} \propto h$ and $u_{j-1/2} - u_{j+1/2} \propto h$,

$$\int_{y_{j-1/2}}^{y_{j+1/2}} \phi(y)u(y)\mathrm{d}y = {}^{y}(\phi u)_j^{\mathrm{LI}} + O(h^5). \tag{A.16}$$

This expression is fifth-order accuracy. The integration method (50) also has fifth-order truncation error respect to mesh size h_x in the x-direction. However, the derivatives includes fourth-order truncation error for h_y in the y-direction as shown in Appendix 1. Then the integration method (50) can be expressed as

$$\int_{x_{i-1/2}}^{x_{i+1/2}} \frac{\partial \phi v}{\partial y}\mathrm{d}x = {}^{x}\left(\frac{\partial \phi v}{\partial y} \right)_i^{\mathrm{LI}} + O_y(h_y^4) + O_x(h_x^5). \tag{A.17}$$

Appendix 6. Artificial viscosity for inviscid compressible fluid

In computations of inviscid compressible fluid, we add an artificial viscosity to the compressed region. The artificial viscosity is included as an additional term in the momentum conservation equations:

$$\left(\frac{\partial^x m}{\partial t} \right)_i = -\left(mu + p + \kappa \frac{\partial m}{\partial x} \right)_{i+1/2} + \left(mu + p + \kappa \frac{\partial m}{\partial x} \right)_{i-1/2}, \tag{A.18}$$

$$\left(\frac{\partial m}{\partial t} \right)_{i+1/2} = -\frac{\partial}{\partial x}\left(mu + p - \kappa \frac{\partial m}{\partial x} \right)_{i+1/2}, \tag{A.19}$$

where the notation κ represents the artificial viscous coefficient:

$$\kappa_{i+1/2} = \begin{cases} 0 & {}^{x}u_{i+1} \geqslant {}^{x}u_i \\ \kappa_0 & {}^{x}u_{i+1} < {}^{x}u_i \end{cases}. \tag{A.20}$$

In this paper, we set the coefficient $\kappa_0 = 0.1h$ for both the one- and two-dimensional Riemann problems. Although diffusion terms in the Navier–Stokes Eq. (53) are solved by using the central discretizations (11) and (12), the artificial viscous terms are discretized as follows:

$$\left(\frac{\partial m}{\partial x} \right)_{i+1/2} = \frac{{}^{x}m_{i+1} - {}^{x}m_i}{h^2}, \tag{A.21}$$

$$\left(\frac{\partial^2 m}{\partial x^2} \right)_{i+1/2} = \frac{3}{h^3}({}^{x}m_{i+1} + {}^{x}m_i) - \frac{6}{h^2} m_{i+1/2}. \tag{A.22}$$

These expressions are derived from the second-order polynomial Φ^{A} determined by the three constraints of $\Phi^{\mathrm{A}}(0) = \phi_{i+1/2}$, $\int_{-h}^{0} \Phi^{\mathrm{A}}\,\mathrm{d}X = {}^{x}\phi_i$, and $\int_{0}^{h} \Phi^{\mathrm{A}}\,\mathrm{d}X = {}^{x}\phi_{i+1}$.

References

[1] T. Yabe, T. Aoki, A universal solver for hyperbolic equations by cubic-polynomial interpolation I. One-dimensional solver, Comput. Phys. Commun. 66 (1991) 219–242.

[2] T. Yabe, F. Xiao, T. Utsumi, The constrained interpolation profile method for multiphase analysis, J. Comp. Phys. 169 (2001) 556–593.

[3] T. Utsumi, T. Aoki, T. Kunugi, Stability and accuracy of the cubic interpolated propagation scheme, Comput. Phys. Commun. 101 (1997) 9–20.
[4] T. Yabe, K. Takizawa, F. Xiao, T. Aoki, T. Himeno, T. Takahashi, A. Kunimatsu, A new paradigm of computer graphics by universal solver for solid, liquid, and gas, JSME Int. J. B 47 (2004) 656–663.
[5] T. Utsumi, T. Yabe, J. Koga, T. Aoki, M. Sekine, Accurate basis set by the CIP method for the solutions of Schrödinger equation, Comput. Phys. Commun. 157 (2004) 121–138.
[6] K. Takizawa, T. Yabe, M. Chino, T. Kawai, K. Wataji, H. Hashimoto, T. Watanabe, Simulation and experiment on swimming fish and skimmer by CIP method, Comput. Struct. 83 (2005) 397–408.
[7] T. Himeno, T. Watanabe, A. Konno, Numerical analysis for propellant management in rocket tanks, J. Propul. Power 21 (2005) 76–86.
[8] S. Moriguchi, A. Yashima, K. Sawada, R. Uzuoka, M. Ito, Numerical simulation on flow failure of geomaterials based on fluid dynamics, Soils Fund. 45 (2005) 155–166.
[9] T. Aoki, Interpolated differential operator (IDO) scheme for solving partial differential equations, Comput. Phys. Commun. 102 (1997) 132–146.
[10] K. Sakurai, T. Aoki, W.H. Lee, K. Kato, Poisson equation solver with fourth-order accuracy by using interpolated differential operator scheme, Comput. Math. Appl. 43 (2002) 621–630.
[11] S.K. Lele, Compact finite difference schemes with spectral-like resolution, J. Comput. Phys. 103 (1992) 16–42.
[12] Y. Imai, T. Aoki, Accuracy study of the IDO scheme by Fourier analysis, J. Comput. Phys. 217 (2006) 453–472.
[13] Y. Imai, T. Aoki, Stable coupling between vector and scalar variables for the IDO scheme on collocated grids, J. Comput. Phys. 215 (2006) 81–97.
[14] K. Kato, T. Aoki, S. Kubota, M. Yoshida, A numerical scheme for strong blast wave driven by explosion, Int. J. Numer. Meth. Fluids 51 (2006) 1335–1353.
[15] D. Gaitonde, J.S. Shang, Optimized compact-difference-based finite-volume schemes for linear wave phenomena, J. Comput. Phys. 138 (1997) 617–643.
[16] M.H. Kobayashi, On a class of Padé finite volume methods, J. Comput. Phys. 156 (1999) 137–180.
[17] J.M.C. Pereira, M.H. Kobayashi, J.C.F. Pereira, A fourth-order-accurate finite volume compact method for the incompressible Navier–Stokes solutions, J. Comput. Phys. 167 (2001) 217–243.
[18] R. Tanaka, T. Nakamura, T. Yabe, Constructing exactly conservative scheme in a non-conservative form, Comput. Phys. Commun. 126 (2000) 232–243.
[19] T. Yabe, R. Tanaka, T. Nakamura, F. Xiao, An exactly conservative semi-Lagrangian scheme (CIP–CSL) in one dimension, Mon. Wea. Rev. 129 (2001) 332–344.
[20] T. Nakamura, R. Tanaka, T. Yabe, K. Takizawa, Exactly conservative semi-Lagrangian scheme for multi-dimensional hyperbolic equations with directional splitting technique, J. Comput. Phys. 147 (2001) 171–207.
[21] F. Xiao, A simple CIP finite volume method for incompressible flow, JSME Int. J. B 47 (2004) 664–671.
[22] F. Xiao, A. Ikebata, An efficient method for capturing free boundaries in multi-fluid simulations, Int. J. Numer. Meth. Fluid 42 (2003) 187–210.
[23] F.H. Harlow, J.E. Welch, A numerical calculation of time dependent viscous incompressible flow of fluid with free surface, Phys. Fluid 8 (1965) 2182–2189.
[24] A.A. Amsden, F.H. Harlow, A simplified MAC technique for incompressible fluid flow calculations, J. Comput. Phys. 6 (1970) 322–325.
[25] H. van de Vorst, Bi-CGSTAB: a fast and smoothly converging variant of Bi-CG for the solution of non-symmetric linear system, SIAM J. Sci. Stat. Comput. 13 (1992) 631–644.
[26] P.C. Chu, C. Fan, A three-point combined compact difference scheme, J. Comput. Phys. 140 (1998) 370–399.
[27] G.A. Sod, A survey of several finite difference methods for systems of nonlinear hyperbolic conservation laws, J. Comput. Phys. 27 (1978) 1–31.
[28] F. Xiao, T. Yabe, X. Peng, H. Kobayashi, Conservative and oscillation-less atmospheric transport schemes based on rational functions, J. Geophys. Res. 107 (2002) 4609–4619.
[29] C.W. Schulz-Rinne, J.P. Collins, H.M. Glaz, Numerical solution of the Riemann problem for two-dimensional gas dynamics, SIAM J. Sci. Comput. 14 (1993) 1394–1414.
[30] P.D. Lax, X.-D. Liu, Solution of two-dimensional Riemann problems of gas dynamics by positive schemes, SIAM J. Sci. Comput. 19 (1998) 319–340.
[31] A. Kurganov, E. Tadmor, Solution of two-dimensional Riemann problems for gas dynamics without Riemann problem solvers, Numer. Meth. PDEs 18 (2002) 584–608.
[32] H.J. Schroll, Relaxed high resolution schemes for hyperbolic conservation lows, SIAM J. Sci. Comput. 21 (2004) 251–279.
[33] D. Gottlieb, A. Orszag, Numerical Analysis of Spectral Methods, SIAM, Philadelphia, 1977.
[34] U. Ghia, K.N. Ghia, C.T. Shin, High-Re solution for incompressible flow using the Navier–Stokes equations and a multigrid method, J. Comput. Phys. 48 (1982) 387–411.